Muscovite ^{40}Ar/^{39}Ar and *in situ* sulfur isotope analyses of the slate-hosted Gutaishan Au–Sb deposit, South China: Implications for possible Late Triassic magmatic-hydrothermal mineralization

Wei Li[a,b], Gui-Qing Xie[b,*], Jing-Wen Mao[b], Zhi-Yuan Zhang[b], Bin Fu[c], Song Lu[d]

[a] *Faculty of Earth Resources, China University of Geosciences, Wuhan 430074, China*
[b] *Key Laboratory of Metallogeny and Mineral Assessment, Institute of Mineral Resources, Chinese Academy of Geological Sciences, Beijing 100037, China*
[c] *Research School of Earth Sciences, The Australian National University, Canberra, ACT 0200, Australia*
[d] *School of Earth Sciences, The University of Melbourne, Victoria 3010, Australia*

ABSTRACT

The Gutaishan deposit is a slate-hosted Au–Sb deposit in the Xiangzhong metallogenic province, South China. The deposit has proven reserves of ca. 9 tonnes (t) of gold with an average grade of 13 g/t and 2,500 t of Sb with an average grade of 10%. In this study, muscovite ^{40}Ar/^{39}Ar and *in situ* sulfur isotope analyses of pyrite and arsenopyrite were performed to determine the mineralization age and the plausible source of S and Au. The ^{40}Ar/^{39}Ar dating result of muscovite limits the formation age of the Gutaishan deposit to ca. 223.6 ± 5.3 Ma, coeval with the adjacent Baimashan granite (223–204 Ma). The *in situ* ^{34}S values of pyrite and arsenopyrite coexisting with native gold lie in a range between −3.7 and +2.1‰ with a mean value of -0.8‰, and these values are markedly different from those of sedimentary pyrite (+7.0 to +23.3‰), indicating a contribution from magmatic sulfur. A magma-derived genetic model may therefore be suitable for the Gutaishan deposit. Integrating the available ages of the Au–Sb and Sb–Au deposits and granites in the Xiangzhong metallogenic province, we propose that a widespread Late Triassic magmatic-hydrothermal Au–Sb mineralization event occurred.

1. Introduction

Orogenic and intrusion-related gold deposits represent two economically important types of gold deposits, and the auriferous quartz veins in both of these systems can occur in metamorphic rocks (Groves et al., 1998; Sillitoe and Thompson, 1998; Lang and Baker, 2001; Groves et al., 2003; Robert et al., 2007). Considerable confusion is often encountered when differentiating these two deposit types due to similarities in their fluid inclusions (e.g., low salinity, aqueous carbonic composition; Ridley and Diamond, 2000; Baker, 2002), wall-rock alterations and sulfide mineral assemblages (Sillitoe and Thompson, 1998; Lang and Baker, 2001; Groves et al., 2003; Goldfarb et al., 2005). For example, both intrusion-related and orogenic genetic models have been suggested for the Muruntau gold deposit in Uzbekistan, which constitutes one of the largest known examples of this type of deposit worldwide (Thompson and Newberry, 2000; Groves et al., 2003; Morelli et al., 2007). Similarly, for the Clear Creek gold occurrences in the Tintina Gold Province, Canada, robust Re-Os molybdenite and ^{40}Ar/^{39}Ar geochronology dates of hydrothermal micas (coeval with

intrusion) in conjunction with sulfur isotope results (Marsh et al., 2003; Selby et al., 2003) confirmed a magmatic-hydrothermal origin rather than an orogenic origin as previously proposed (Goldfarb et al., 2004). Furthermore, Xue et al. (2013) performed *in situ* sulfur isotope study on four Archean gold deposits, the results of which were consistent with auriferous fluids originating from a felsic magma or mantle source in contrast to the metamorphic hypothesis (Phillips and Powell, 2010). Hence, establishing an unequivocal absolute age for mineralization coupled with isotope signatures is critical for testing the ore genesis of these deposits (Kerrich and Cassidy, 1994; Rice et al., 2016).

Pyrite and arsenopyrite are highly efficient repositories of invisible gold in gold deposits (Cook and Chryssoulis, 1990). Advances in *in situ* sulfur isotope analysis permit a precise determination of sulfur isotope signatures across zoned crystals or finely intergrown sulfides from different provenances (Kesler et al., 2005; Barker et al., 2009; Peterson and Mavrogenes, 2014; Chen et al., 2015; Tanner et al., 2016). For example, the δ^{34}S values for a zoned pyrite grain acquired from the Porgera gold deposit, Papua New Guinea, range from −11.98 to +0.34‰ (Peterson and Mavrogenes, 2014); the δ^{34}S values in pyrites

* Corresponding author at: Institute of Mineral Resources, Chinese Academy of Geological Sciences, No. 26 Baiwanzhuang Road, Beijing 100037, China.
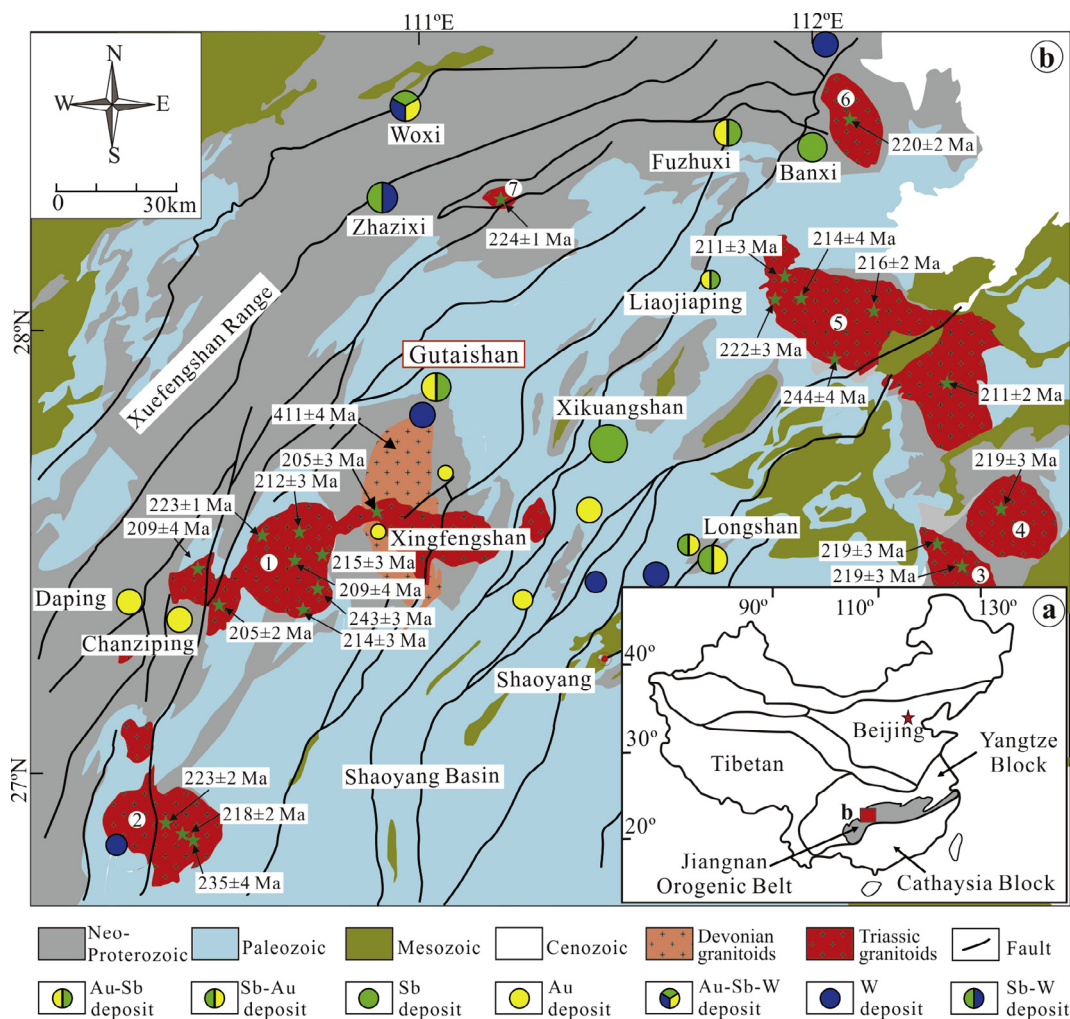E-mail address: xieguiqing@cags.ac.cn (G.-Q. Xie).

Fig. 1. Geological map of the Xiangzhong metallogenic province showing the most important ore deposits and intrusions. Fig. 1a is modified after Wang et al. (2014) and Xu et al. (2017). Fig. 1b is modified after the Geological map of Hunan province, the People's Republic of China (2010), and Chu et al. (2012b). The numbers represent the granites: 1–Baimashan, 2–Wawutang, 3–Ziyunshan, 4–Xiema, 5–Weishan, 6–Taojiang, 7–Dashenshan.

from the sediment-hosted Qiuling gold deposit in China range from −27.1 to +69.6‰ (Chen et al., 2015). These large variations in sulfur compositions suggest that the interpretations of sulfur isotope data obtained by conventional bulk powder methods may be problematic or potentially misleading. This recognition provides much-needed insight into the sources of sulfur and the changes in the physiochemical conditions, particularly the pressure and oxygen fugacity, during sulfide precipitation.

The Xiangzhong metallogenic province (XZMP), which is located on the southeastern part of the Yangtze Block, South China (Fig. 1a), is one of the most important Sb–Au metallogenic belts in China (Hu and Zhou, 2012; Mao et al., 2013; Hu et al., 2017a; Xie et al., 2018a, b). The genesis of the slate-hosted Au–Sb and Sb–Au deposits in the XZMP has long been controversial, and both intrusion-related and intrusion-unrelated models have been proposed, as reviewed by Hu et al. (2017b). This debate is mainly due to the lack of reliable mineralization ages in these Au–Sb and Sb–Au deposits and to the absence of intrusions within the mining district (Hu et al., 2016, 2017b).

In this study, we focus on the slate-hosted Gutaishan Au–Sb deposit located in the XZMP. Available studies on this deposit have been conducted on fluid inclusions, H–O–C stable isotopes (Li et al., 2016), and trace element compositions in pyrite and arsenopyrite (Li et al., 2018). The results of these investigations demonstrated that the Gutaishan deposit is fault-controlled, that the ore-forming fluids have an aqueous carbonic composition and low salinity, and that the pyrite and

arsenopyrite exhibit complex overgrowth textures (Li et al., 2018). We present new data consisting of muscovite $^{40}Ar/^{39}Ar$ ages and in situ sulfur isotope analyses of pyrite and arsenopyrite to (1) constrain the mineralization age, (2) trace the plausible source of the S and Au, and (3) compile available data for the Sb–Au and Au–Sb deposits to obtain new insights into their formation mechanism.

2. Regional geological setting

The XZMP, which is located in the southeastern part of the Yangtze Block (Fig. 1a), is one of the most important Sb–Au metallogenic belts in China (Hu and Zhou, 2012; Mao et al., 2013; Hu et al., 2016). The XZMP hosts more than 170 Sb and Au deposits and occurrences (Hu et al., 2017b), including the world's largest Xikuangshan Sb deposit, the Gutaishan Au–Sb and Longshan Sb–Au deposits (Fig. 1b). These deposits are composed of ore-bearing quartz or calcite veins that are controlled by faulting and folding (Peng et al., 2003; Li et al., 2016; Hu et al., 2017b). The vein mineralogy is generally simple in these deposits; for example, quartz, pyrite, arsenopyrite and stibnite are the dominant minerals in the Gutaishan Au–Sb deposit and Longshan Sb–Au deposit (Liu et al., 2008; Li et al., 2016), and quartz, calcite and stibnite are the major minerals in the Xikuangshan Sb deposit (Peng et al., 2003).

Strata exposed in the XZMP consist mainly of Neoproterozoic metamorphic basement and Paleozoic to Cenozoic sedimentary rocks
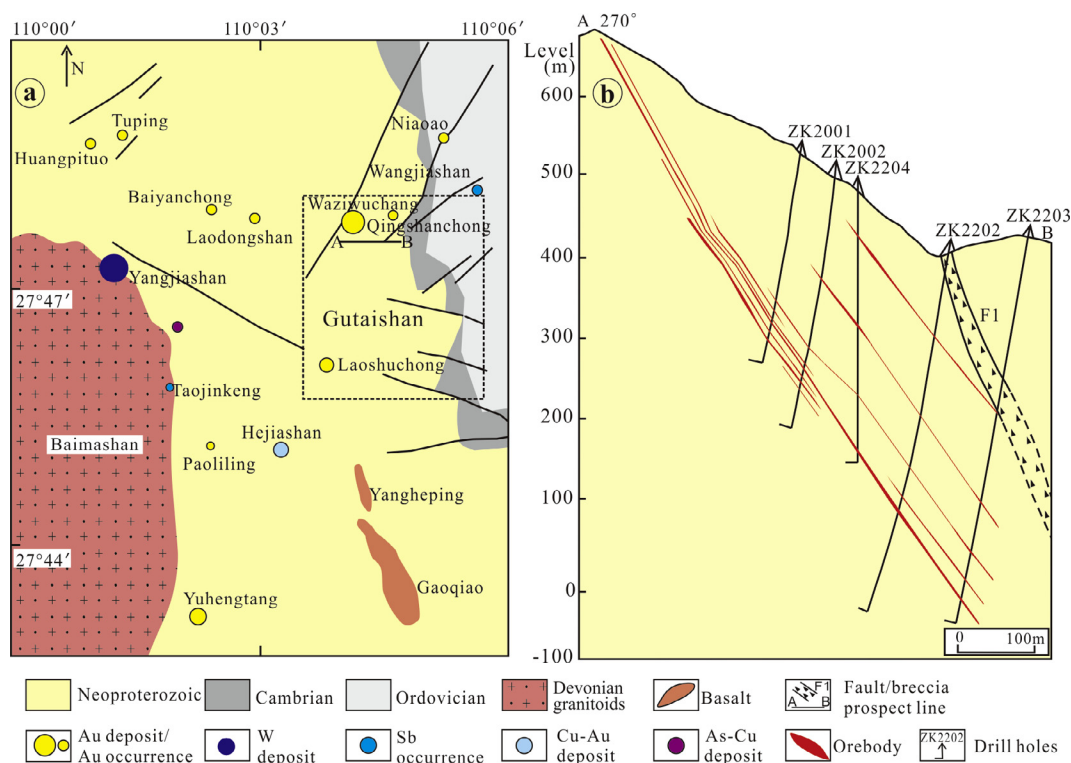
Fig. 2. a Sketched geological map of the Gutaishan ore field and its adjacent areas. b Cross-section through the Gutaishan deposit. The map is modified after Li et al. (2016).
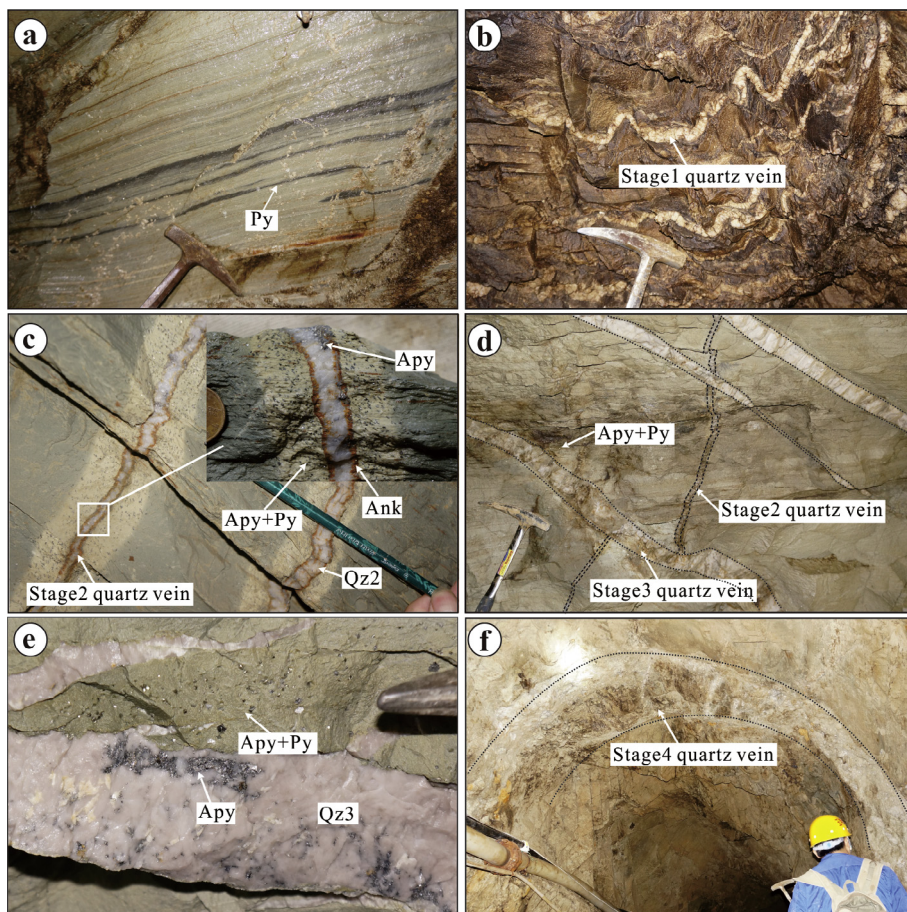

Fig. 3. Photographs illustrating the characteristics of different stages of quartz veins and sulfides from the Gutaishan deposit. a Stratiform sedimentary pyrite veins within the Banxi Group. b Deformed Stage 1 quartz veins within the "dirty" Banxi Group. c Swarms of Stage 2 quartz-sulfide veins within the Banxi Group. Note the abundance of arsenopyrite and pyrite within the discoloured wall rock, whereas ankerite is mainly located in the contact zone. d Cross-cutting relationships between Stage 2 and Stage 3 quartz veins. Note that arsenopyrite and pyrite are well developed within the wall rock adjacent to both stages of quartz veins. e Quartz-sulfide veins in Stage 3. The arsenopyrite and pyrite are located in both veins and wall rock. f Stage 4 post-ore quartz vein filling a fault. Abbreviations: Ank–ankerite, Apy–arsenopyrite, Py–pyrite, Qz–quartz.

Table 1
Characteristics of auriferous quartz veins in Stage 3 in the Gutaishan deposit.

| Type	Strike	Dip	Level (m)	Strike length (m)	Width (cm)	Major minerals	Type of sulfides	Gold grade	Wallrock alteration
1	NW–N	NE	0–715	100–250	20–100	quartz, arsenopyrite, pyrite, ankerite, native gold, bournonite, jamesonite, tetrahedrite, scarce galena and sphalerite, chalcopyrite	Py3a, Apy3a	5–375 g/t, local > 10,000 g/t	sulfidation and carbonatization
2	NW–N	NE	50–500	100–250	5–15	quartz, ankerite, scarce native gold	Py3a, Apy3a	2–10 g/t	sulfidation and carbonatization
3	NW	SW	360	unknown	5–25	quartz, arsenopyrite, pyrite, scarce native gold	Py3b, Apy3b	1–10 g/t	silicification
4	NW	NE	> 480	unknown	20–80	quartz, stibnite, ankerite, pyrite, scarce native gold	Py3c, Py3d	Au: 2–15 g/t; Sb: 0.5–13%	sulfidation
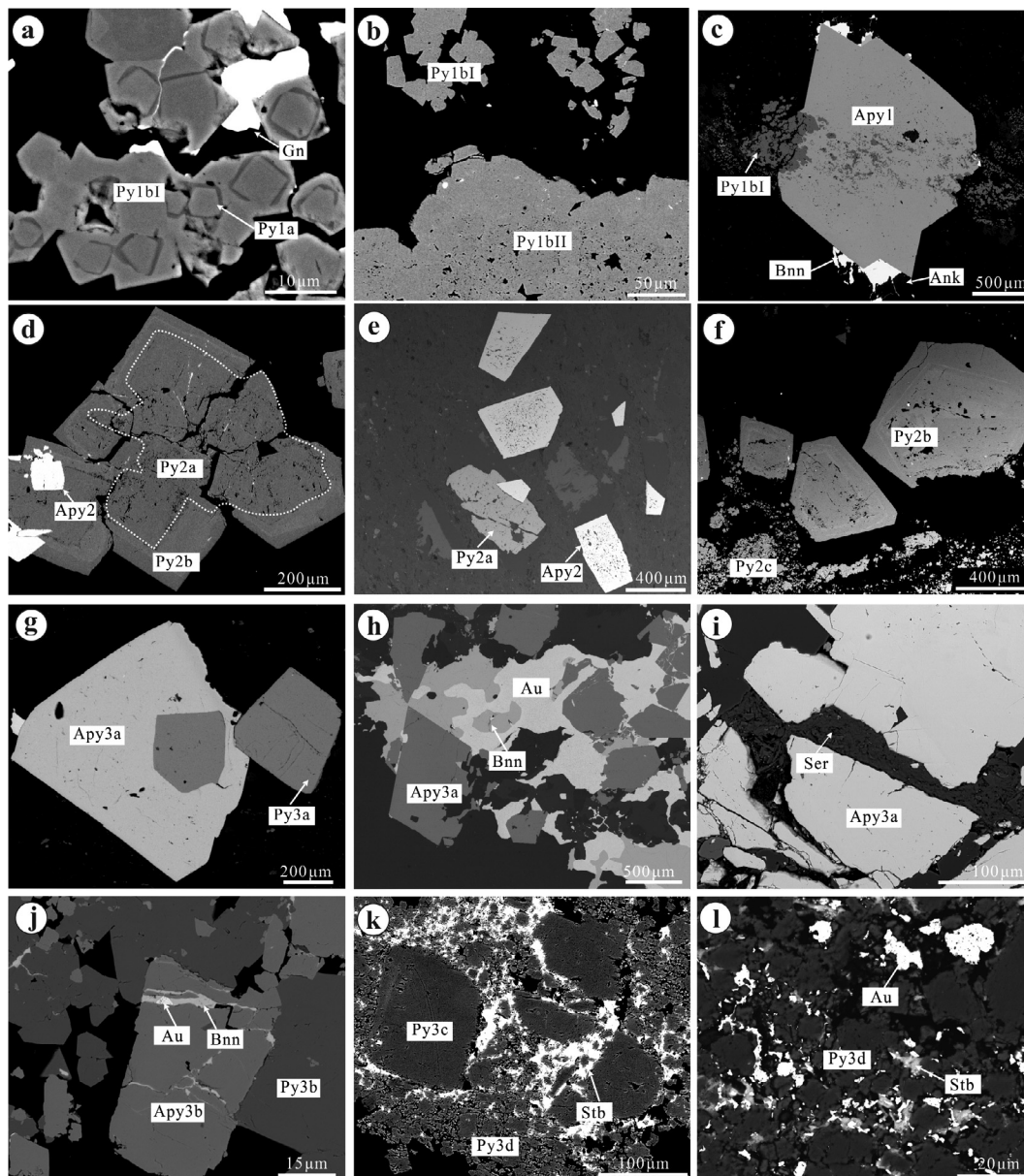
Fig. 4. Back-scattered electron (BSE) images showing textural features of pyrite and arsenopyrite in different stages. a Cluster of Py1a microcrystals surrounded by Py1bI. b Textural features of a different occurrence of Py1b. c Euhedral coarse-grained arsenopyrite grain replaced by Py1bI. Bournonite and ankerite are located along the margin. d Py2a with porous texture overgrown by zoned subhedral Py2b within a quartz vein. e Euhedral porous Apy2 coexisting with porous Py2a within the wall rock. f Fine-grained Py2c clusters overgrowing euhedral coarse-grained Py2b. g Subhedral Apy3a intergrown with Py3a. h Coarse-grained native gold coexisting with Apy3a and bournonite. i Fine-grained sericite filling microfractures in Apy3a. j Apy3b coexisting with Py3b and fine-grained gold within Apy3b. k Different occurrence of pyrite in a stibnite-dominated vein. Coarse-grained Py3c cemented by fine-grained Py3d; both are infilled by stibnite. l Fine-grained native gold coexisting with stibnite. Abbreviations: Ank–ankerite, Apy–arsenopyrite, Au–native gold, Bnn–bournonite, Gn–galena, Py–pyrite, Ser–sericite, Stb–stibnite.
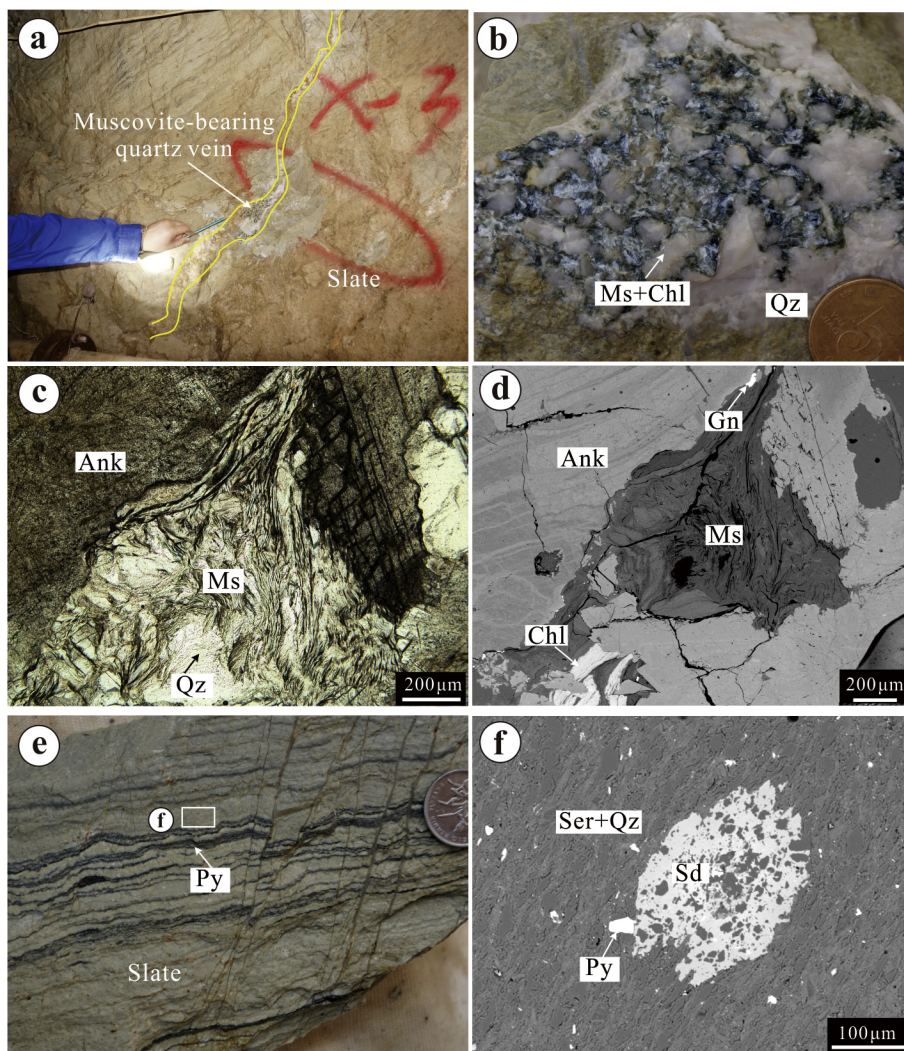
Fig. 5. Photographs showing the occurrences and micro textures of muscovite and sericite in the Gutaishan deposit. a–d Muscovite-bearing auriferous quartz vein. Within the vein, ankerite and chlorite coexist with muscovite. e, f Pyrite-bearing slate; the pyrite thin layer spreads within the slate. Microscopic observations show minor siderite coexisting with sericite. Abbreviations: Ank–ankerite, Chl–chlorite, Gn–galena, Ms–muscovite, Py–pyrite, Sd–siderite, Ser–sericite, Qz–quartz.

(Fig. 1b). The Neoproterozoic rocks are part of the crystalline basement of the South China Craton and serve as the basic rock units for the Jiangnan orogenic belt (Fig. 1a). The Neoproterozoic strata include three units: the Lengjiaxi and Banxi Groups and the Jiangkou Formation. The protoliths of the Lengjiaxi and Banxi Groups are mostly slate and clastic rocks, while the Jiangkou Formation mainly consists of conglomerate, sandstone, siltstone, shale, and carbonate rocks. These basement rocks compose the majority of the wall rock for the Sb–Au and Au–Sb deposits (Ma et al., 2002; Hu et al., 2017b).

Tectonically, the XZMP is situated within the Xuefengshan belt (Chu et al., 2012a, Hu et al., 2017b), which is characterized by large-scale fold and thrust structures and widespread granites. The Early Paleozoic Caledonian orogeny produced ductile shearing, intense folding, and granitic magmatism within this belt (Faure et al., 2009); for example, published zircon U–Pb geochronology results show that the Early Paleozoic Baimashan granite exhibits concordia U–Pb zircon ages of 411 ± 4 Ma (Chu et al., 2012b) and 407 ± 3 Ma (Xie et al., 2018a). Subsequently, the Xuefengshan belt was significantly affected by the Indosinian orogeny, the tectonism of which was characterized by well-developed thrust faults, folds and ductile syn-metamorphic deformation

(Wang et al., 2005) in addition to the emplacement of granitic plutons. Recent geochronological data show that ductile shearing occurred between 243 and 226 Ma (Chu et al., 2012a). Triassic granitic rocks crop out within the Xuefengshan belt. As shown in Appendix Table 1 (Table A1), these Triassic granites were emplaced in two stages: between ~245 Ma and 228 Ma; subsequently, from 220 to 206 Ma (Wang et al., 2007; Chu et al., 2012b; Fu et al., 2015; Gao et al., 2017).

3. Ore deposit geology

The Gutaishan Au–Sb deposit, which is located to the northeast of the Baimashan batholith (Fig. 1b), contains proven reserves of 9 tonnes (t) of Au and 2,500 t of Sb. The average grade of the gold ore is approximately 13 g/t, although the grades of local bonanza-grade ores reach 10,000 g/t. The average Sb content of the stibnite-dominant ores is ~10% (Li et al., 2016, 2018).

The country rocks include Neoproterozoic and Cambrian–Ordovician strata, where the former constitutes the major host rock for auriferous quartz veins (Fig. 2). The Neoproterozoic strata consist of grey-green silty slates and light green bedded slate. Thin

Table 2
Argon isotope compositions of muscovite in the Gutaishan deposit.

Sample No.	Step No.	Laser power	^{40}Ar(fA)	±1σ	^{39}Ar(fA)	±1σ	^{38}Ar(fA)	±1σ	^{37}Ar(fA)	±1σ	^{36}Ar(fA)	±1σ	^{39}Ar($\times10^{-14}$)	Ca/K	%^{40}Ar*	^{40}Ar*/^{39}Ar	±1σ	Cum.% ^{39}Ar	Apparent Age (Ma)	±1σ
GTS-230-1a	1	0.005	2343.05	0.68	8.232	0.014	1.4677	0.0017	0.38	0.0088	7.7860	0.16	0.0292	0.081	0.8	2.2424	0.3309	6.40	124.87	17.80
GTS-230-1b	2	0.008	1242.22	0.62	37.923	0.016	0.6806	0.0011	1.73	0.0056	3.6106	0.17	0.1346	0.080	13.2	4.3308	0.0473	35.88	233.87	2.39
GTS-230-1c	3	0.012	348.22	0.12	52.542	0.027	0.0816	0.0001	1.25	0.0006	0.4329	0.15	0.1865	0.042	62.9	4.1678	0.0045	76.73	225.59	0.23
GTS-230-1d	4	0.016	126.98	0.02	23.656	0.007	0.0206	0.0001	0.65	0.0007	0.1094	0.17	0.0840	0.048	74.3	3.9875	0.0084	95.12	216.40	0.43
GTS-230-1e	5	0.02	20.33	0.01	3.594	0.011	0.0035	0.0001	0.30	0.0003	0.0185	0.10	0.0128	0.147	72.9	4.1226	0.0313	97.91	223.29	1.59
GTS-230-1f	6	0.03	11.25	0.02	2.065	0.016	0.0017	0.0001	0.03	0.0003	0.0093	0.17	0.0073	0.025	75.4	4.1059	0.0539	99.52	222.44	2.75
GTS-230-1g	7	0.1	7.00	0.03	0.619	0.015	0.0028	0.0001	0.21	0.0006	0.0148	0.19	0.0022	0.584	37.0	4.1915	0.2965	100.00	226.80	15.07

Note: Data are corrected for mass spectrometer backgrounds, discrimination, radioactive decay and interference corrections. Interference corrections: $(^{36}Ar/^{37}Ar)_{Ca} = (2.5782 \pm 0.0018) \times 10^{-4}$; $(^{39}Ar/^{37}Ar)_{Ca} = (6.5620 \pm 0.0164) \times 10^{-4}$; $(^{40}Ar/^{39}Ar)_{K} = (1.00 \pm 0.05) \times 10^{-10}$; $(^{38}Ar/^{39}Ar)_{K} = (1.2246 \pm 0.0028) \times 10^{-2}$, J-value is 0.031960 ± 0.000011 (0.035%;1σ), based on an age of 28.1260 ± 0.0093 Ma (1σ) for FC sanidine (Phillips et al., 2017). Errors are one sigma uncertainties and exclude uncertainties in the J-value.

pyrite layers showing several to tens of mm thick and oriented parallel to the bedding are abundant (Fig. 3a). The Cambrian–Ordovician strata are distributed along the eastern margin of the mining district and are composed mainly of carbonaceous mudstone and muddy limestone.

Based on the cross-cutting relationships and mineral assemblages of quartz veins, four distinct mineralization stages are recognized in the Gutaishan deposit (Fig. 3). The pre-ore Stage 1 is represented by the presence of pyrite layers (5–15 mm in thickness) oriented parallel to the bedding in sedimentary rocks (Fig. 3a) and deformed segregation quartz veins that are several to tens of cm thick (Fig. 3b). Stage 2 is marked by thin NW-striking and SW-dipping quartz–ankerite–sulfide veins that are 1 to 20 cm in width (Fig. 3c). Stage 3 represents the main gold–stibnite stage with swarms of auriferous quartz veins in slate (Fig. 3d–e). Post-ore Stage 4 quartz veins with widths ranging from 0.5 to 1.0 m are composed of quartz and dip steeply to the north (Fig. 3f). Four different occurrences of auriferous quartz veins with different mineral assemblages are recognized in Stage 3. Type 1 is mainly composed of quartz, arsenopyrite, pyrite, ankerite, sulfosalts (e.g., bournonite), and visible gold in addition to minor galena, sphalerite and chalcopyrite; type 2 is composed of quartz, ankerite and scarce visible gold; type 3 is composed of quartz and minor pyrite, arsenopyrite and visible gold; and type 4 is dominated by quartz and stibnite with minor pyrite and scarce visible gold. Their principal features are summarized in Table 1.

4. Occurrence of pyrite and arsenopyrite

Nine and four texturally distinct varieties of pyrite and arsenopyrite, respectively, are recognized in the first three stages under reflected light and in back-scattered electron (BSE) images (Fig. 4). The detailed sample characteristics of pyrite and arsenopyrite involved in this study, including their mineral assemblages, are summarized in Table A2. Their textural characteristics are briefly summarized below.

The pyrite from Stage 1 is represented by euhedral to anhedral fine-grained (< 3 μm) pyrite (Py1a) and coarse-grained recrystallized pyrite assemblages (Py1b) (Fig. 4a). Two textural styles of Py1b that commonly overgrow Py1a are observed: subhedral fine-grained homogeneous Py1bI ranging in size from 50 to 100 μm and poorly crystalline homogeneous Py1bII (Fig. 4b) with assemblages greater than 1500 μm in length. Minor subhedral arsenopyrite (Apy1), which is replaced by Py1bI, is recognized in Stage 1 (Fig. 4c).

Three distinct types of pyrite are recognized in Stage 2 (Fig. 4d–f). Py2a occurs as euhedral to anhedral coarse grains that are tens to hundreds of μm in size (Fig. 4d, e). Py2b is generally a few hundreds of μm in size and shows irregular bright inner rims and dark outer rims in BSE images (Fig. 4d). Py2c is anhedral and fine-grained and ranges from several to tens of μm in size (Fig. 4f). The arsenopyrite (Apy2) from Stage 2 appears homogeneous in BSE images and varies from tens to thousands of μm in size (Fig. 4e).

Four types of pyrite and two types of arsenopyrite are identified from the four types of auriferous quartz veins in Stage 3 (Fig. 4g–l, Table 1). Py3a occurs as euhedral to subhedral grains ranging from hundreds of μm to several mm in size (Fig. 4 g). Py3b is commonly sub- to anhedral and ranges from tens to hundreds of μm with homogeneous textures in BSE images, and it either exhibits sharp boundaries with Apy3b or encloses fine-grained Apy3b (Fig. 4j). Py3c has a characteristic oscillatory zoning texture with porous cores that are several hundreds of μm in diameter (Fig. 4k). Py3d is anhedral, homogeneous in BSE images, and generally no more than a few tens of μm in size, and it coexists with stibnite (Fig. 4k, l). Apy3a ranges from hundreds to thousands of μm in size, and it coexists with native gold, sulfosalts (e.g., bournonite), pyrite and muscovite (Fig. 4g–i). Apy3b is subhedral to anhedral and shows a uniform composition in BSE images, and it ranges from tens to hundreds of μm in width (Fig. 4j).
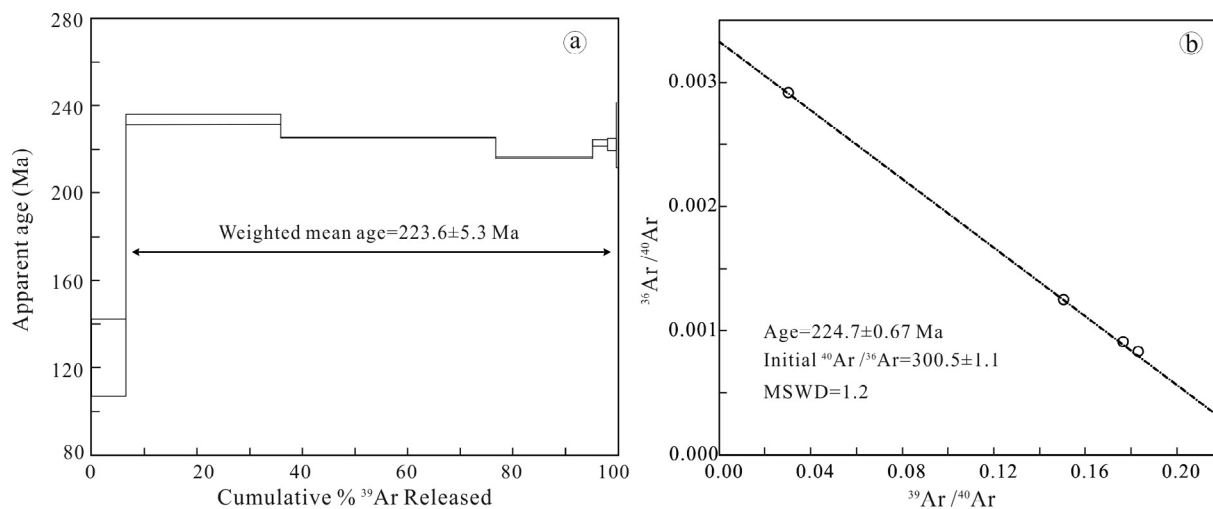
Fig. 6. a ^{40}Ar/^{39}Ar age spectra. b Reverse isochrons in muscovite in the Gutaishan deposit.

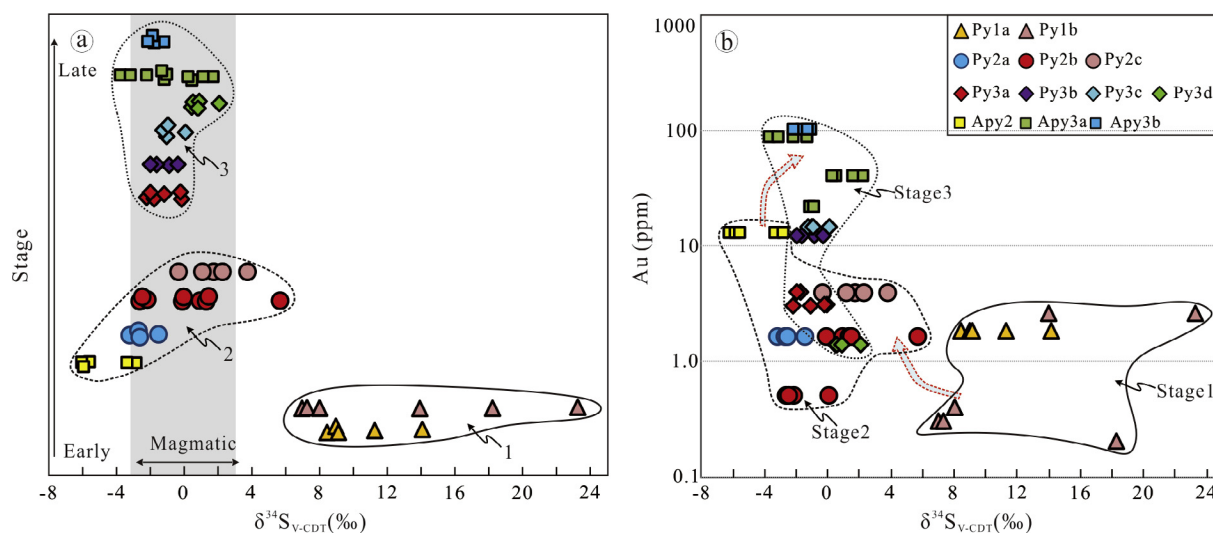**Fig. 7.** a Variations in the δ^{34}S values in different stages. b Au vs. δ^{34}S values for pyrite and arsenopyrite in different stages in the Gutaishan deposit.

5. Samples and analytical methods

One muscovite sample collected from an auriferous quartz vein in an adit at 280 m was selected for ^{40}Ar/^{39}Ar dating. All muscovite grains were carefully handpicked under a binocular microscope after the samples had been crushed and cleaned. ^{40}Ar/^{39}Ar dating was performed in the Noble Gas Laboratory of the School of Earth Sciences at the University of Melbourne, Australia, using a new-generation, multi-collector Thermo Fisher Scientific ARGUS VI mass spectrometer linked to a stainless-steel gas extraction/purification line and Photon Machines Fusions 10.6 CO_2 laser system. The new generation of multi-collector ARGUS VI mass spectrometers provides ultra-high precision measurements with uncertainties of less than 0.1%. The analytical procedures for ARGUS VI systems are described in detail by Phillips and Matchan (2013) and Phillips et al. (2017). The ages were calculated assuming an atmospheric ^{40}Ar/^{36}Ar ratio of 298.56 $\pm$ 0.31 (Lee et al., 2006), and a decay constant of $\lambda = 5.543 \times 10^{-10}\,year^{-1}$ was used (Steiger and Jäger, 1977). The plateau ages for the ^{40}Ar/^{39}Ar age spectra were calculated using ISOPLOT (Ludwig, 2003).

In situ S isotope analyses of pyrite and arsenopyrite from eleven representative samples (Table A2) were performed on a sensitive high-resolution ion microprobe (SHRIMP)–II instrument at the Australia National University (ANU) with a spot size of 27 μm. This instrument utilizes the principles of secondary ion mass spectrometry; a detailed description of the system is outlined in Ireland et al. (2014). The pyrite sulfur isotope data were normalized to the accepted Ruttan pyrite standard assuming a δ^{34}S$_{V-CDT}$ value of 1.2‰ (Crowe and Vaughan, 1996), and the arsenopyrite sulfur isotope data were normalized to an arsenopyrite (YJS-65) standard with a δ^{34}S$_{V-CDT}$ value of -1.0‰ (Xie et al., 2018a); all measurements were relative to the Canyon Diablo troilite (CDT). The error for each sulfur isotope ratio was reported at the 2σ confidence level. In addition, sample measurements from every 3 to 4 analyses were bracketed by at least one standard measurement to ensure precision and account for instrumental drift.

Electron probe microanalysis (EPMA) of the muscovite and its co-existing chlorite from the quartz vein (Fig. 5a–d) and sericite from slate

Table 3

A summary of the *in situ* sulfur isotope composition of pyrite and arsenopyrite in the Gutaishan deposit.

Stage	Textural sub-type	n	δ³⁴S (‰, V-CDT)		Au (ppm)	Stage	Textural sub-type	n	δ³⁴S (‰, V-CDT)		Au (ppm)
1	Py1a	5	Average	10.4	1.8	3	Py3b	4	Average	−1.2	12.3
			Max	14.1	4.6				Max	−0.3	27.3
			Min	8.5	0.8				Min	−1.9	2.0
1	Py1b	6	Average	13.0	0.4	3	Py3c	4	Average	−0.8	14.6
			Max	23.3	0.8				Max	0.1	51
			Min	7.0	0.2				Min	−1.2	2.1
2	Py2a	4	Average	−2.4	1.6	3	Py3d	5	Average	1.0	1.4
			Max	−1.4	4.0				Max	2.1	6.1
			Min	−3.2	0.4				Min	0.5	0.2
2	Py2b	9	Average	0.3	0.5	2	Apy2	5	Average	−4.7	13.1
			Max	5.7	1.8				Max	−2.8	85.9
			Min	−2.6	0.1				Min	−5.9	0.2
2	Py2c	5	Average	1.8	3.9	3	Apy3a	10	Average	−0.9	88.7
			Max	3.8	15.9				Max	1.7	203
			Min	−0.3	6.3				Min	−3.7	2.7
3	Py3a	6	Average	−1.2	4.0	3	Apy3b	4	Average	−1.7	102
			Max	−0.1	14.2				Max	−1.3	367
			Min	−2.2	0.6				Min	−2.2	2.9

Note: The contents of Au measured by LA–ICP–MS are after Li et al. 2018.

Table 4

EPMA analytical data for the muscovite and sericite in the Gutaishan deposit (data in wt.%).

Sample No.	GTS-230-7	GTS-230-8	GTS-230-9	GTS-230-10	GTS-230-11	GTS-230-12	GTS-207-3-2	GTS-207-3-4	GTS-207-3-5	GTS-207-3-6
Mineral	muscovite	muscovite	muscovite	muscovite	muscovite	muscovite	sericite	sericite	sericite	sericite
Na₂O	4.19	0.40	2.93	3.98	0.79	1.39	0.78	0.27	1.30	0.54
MgO	0.20	0.53	0.30	0.19	0.46	0.30	0.33	0.81	0.63	0.72
Al₂O₃	39.68	36.75	39.65	39.15	37.27	36.59	34.31	35.11	37.21	35.62
K₂O	2.30	8.64	4.33	2.96	8.61	7.25	8.19	9.86	7.81	8.87
CaO	0.24	0.04	0.16	0.11	0.03	0.06	0.12	0.07	0.07	0.13
SiO₂	49.76	49.95	49.28	47.72	46.84	48.42	46.63	50.74	47.61	48.87
FeOᵀ	0.25	0.36	0.25	0.31	0.41	0.33	0.57	1.10	0.60	0.91
Cr₂O₃	0.06	0.05	0.04	0.13	0.00	0.01	0.19	0.06	0.03	0.06
TiO₂	0.02	0.00	0.01	0.03	0.01	0.01	0.09	0.23	0.09	0.18
Total	96.69	96.71	96.95	94.58	94.43	94.35	91.21	98.24	95.34	95.90

(Fig. 5e, f) was performed using a JEOL JXA-8230 electron probe microanalyser at the Key Laboratory of Metallogeny and Mineral Assessment, Institute of Mineral Resources, Chinese Academy of Geological Sciences, Beijing. All measurements were performed using an accelerating voltage of 15 kV, a beam current of 20 nA, and a beam size of 1 μm. The analyzed standards and average minimum limits of detection were as follows: Si (albite), 83–96 ppm; Ti (TiO₂), 236–244 ppm; Al (albite), 77–81 ppm; Fe (hematite), 87–99 ppm; Mg (MgO), 65–74 ppm; Ca (apatite), 64–77 ppm; Na (albite), 71–87 ppm; K (K-feldspar), 48–53 ppm; and Cr (Cr₂O₃), 112–137 ppm.

6. Results

6.1. ⁴⁰Ar/³⁹Ar age of muscovite

The analytical results are listed in Table 2. The apparent age spectra and inverse isochron age are presented in Fig. 6. In this study, a plateau is defined as a sequence of six consecutive steps that include at least 90% of the total ³⁹Ar released.

The aliquot yields a well-defined plateau age of 223.6 ± 5.3 Ma and an inverse isochron age of 224.7 ± 0.7 Ma (MSWD = 1.2) at an initial ⁴⁰Ar/³⁶Ar ratio of 300.5 ± 1.1 (Fig. 6).

6.2. Sulfur isotope compositions of pyrite and arsenopyrite

A total of 67 sulfur isotope measurements on pyrite and arsenopyrite were obtained, and the results are shown in Fig. 7 and Table 3; the full dataset is provided in Table A3. The measured intra-crystalline δ³⁴S variation exceeds the analytical error in each crystal.

Pyrites from Stage 1 (Py1a and Py1b) are enriched and show a wide variation in δ³⁴S values ranging from 8.5 to 14.1‰ for Py1a (n = 5) and 7.0 to 23.3‰ for Py1b (n = 6).

The δ³⁴S values for the sulfides from Stage 2 (Py2a, Py2b, Py2c and Apy2) fall within a relatively narrow range: −3.2 to −1.4‰ for Py2a (n = 4); −2.6 to 5.7‰ for Py2b (n = 9); −0.3 to 3.8‰ for Py2c (n = 5); and −5.9 to −2.8‰ for Apy2 (n = 5).

The sulfides from Stage 3 (Py3a, Py3b, Py3c, Py3d, Apy3a and Apy3b) exhibit very limited δ³⁴S values that vary from −2.2 to −0.1‰ for Py3a (n = 6), −1.9 to 0.3‰ for Py3b (n = 4), −1.2 to 0.1‰ for Py3c (n = 4), 0.5 to 2.1‰ for Py3d (n = 5), −3.7 to 1.7‰ for Apy3a (n = 10), and −2.2 to −1.3‰ for Apy3b (n = 4).

6.3. Compositions of mica and chlorite

The EPMA results show that the coarse-grained muscovite from the quartz vein (Fig. 5a-d) and the fine-grained sericite from slate (Fig. 5e,

Table 5
EPMA analytical data for the chlorite in the Gutaishan deposit (data in wt.%).

Sample No.	GTS-230-13	GTS-230-14	GTS-230-15	GTS-230-16	GTS-230-17
SiO_2	25.29	23.22	23.70	23.98	23.69
TiO_2	0.01	0.00	0.00	0.00	0.00
Al_2O_3	23.13	22.99	24.00	23.21	23.43
Cr_2O_3	0.36	0.13	0.12	0.13	0.27
FeO^T	30.20	27.17	29.47	29.05	28.38
MnO	0.10	0.06	0.03	0.06	0.02
MgO	9.29	10.55	9.60	9.60	9.62
CaO	0.10	0.03	0.02	0.01	0.01
Na_2O	0.12	0.01	0.00	0.00	0.03
K_2O	0.05	0.02	0.01	0.00	0.00
Total	88.74	84.27	87.13	86.12	84.60
Structural formulas based on 14 oxygen					
Si	2.68	2.58	2.56	2.61	2.59
Al (iv)	1.32	1.42	1.44	1.39	1.41
Al (vi)	1.58	1.59	1.63	1.61	1.63
Ti	0.00	0.00	0.00	0.00	0.00
Cr	0.03	0.01	0.01	0.01	0.02
Fe^{3+}	0.15	0.10	0.11	0.13	0.13
Fe^{2+}	2.53	2.42	2.55	2.52	2.46
Mn	0.01	0.01	0.00	0.01	0.00
Mg	1.47	1.74	1.55	1.56	1.57
Ca	0.01	0.00	0.00	0.00	0.00
Na	0.05	0.00	0.00	0.00	0.01
K	0.01	0.00	0.00	0.00	0.00
T/°C	243.4	253.3	257.4	250.6	252.0

f) display distinct compositions, particularly with regard to Na, K, Fe and Ti, the data are provided in Table 4. For example, the Na_2O contents in the muscovite range from 0.40 to 4.19 wt% with a mean value of 2.28 wt% (n = 6); in contrast, the values in sericite vary from 0.27 to 1.30 wt% with a mean value of 0.72 wt% (n = 4).

The composition of chlorite has a narrow range, i.e., the contents of MgO range from 9.29 to 10.55 wt%, the data for which are provided in Table 5. Applying the chlorite geothermometer from Battaglia (1999), the calculated temperature ranges between 243 and 257 °C (Table 5).

7. Discussion

7.1. Timing of Au–Sb mineralization

In this study, we believe that the $^{40}Ar/^{39}Ar$ age of muscovite can provide constraints on the age of Au mineralization based on the following considerations: (1) the ore grade of this vein is ~1 g/t (communication with the mining company); (2) microscopic observations show that the muscovite precipitated only in Stage 3 (Fig. 4i), and the composition of these analyzed muscovite grains is different from that of the sericite from slate (Table 4), further confirming that the muscovite is of hydrothermal origin; (3) the occurrence of this vein is similar to that of the type 1 auriferous quartz veins in Stage 3, and they are both NW-striking and NE-trending; (4) the mineral assemblage consisting of quartz, muscovite, ankerite, chlorite and galena is consistent with that of the native gold-bearing ores in Stage 3; and (5) the chlorite geothermometer yields temperatures ranging between 243 and 257 °C (Table 5), which are coincident with the fluid inclusion homogenization temperatures within quartz coexisting with native gold in Stage 3 (190–320 °C; Li et al., 2016). All of these temperatures are similar to the closure temperatures of muscovite (300–350 °C; McDougall and Harrison, 1999).

Additionally, the inverse isochron has an initial $^{40}Ar/^{36}Ar$ ratio of

300.5 ± 1.1; this value is similar to the present-day atmospheric ratio (298.56 ± 0.31; Mark et al., 2011), indicating that negligible excess argon was retained in this muscovite grain (Kuiper, 2002). Combining this information with the well-defined plateau age, we suggest that 223.6 ± 5.3 Ma represents the age of Au mineralization.

7.2. Potential magmatic-hydrothermal derived Au and S

The characteristics of the Gutaishan Au–Sb deposit, including its alteration (sulfidation and sericitization), metallic element assemblage (Au + Sb + Bi + W), and fluid inclusion types (CO_2–H_2O ± CH_4, Li et al., 2016), are all consistent with those of orogenic gold deposits (Goldfarb et al., 2005) or are otherwise similar to those of the proximal products of intrusion-related vein gold deposits (Sillitoe and Thompson, 1998; Lang and Baker, 2001). However, integrating the following lines of evidence, we estimate that the largest endowment of Au and S originates from a deeply buried magmatic source.

(1) The lack of sulfate in the Gutaishan deposit indicates that H_2S is the dominant sulfur species or that the hydrothermal fluid was in a relatively reduced oxidation state; therefore, the measured pyrite and arsenopyrite sulfur compositions represent the approximate sulfur isotope composition of the ore-forming fluid (Ohmoto, 1986). The measured ^{34}S values in the pyrite and arsenopyrite coexisting with native gold from Stage 3 range from −3.7 to +2.1‰, overlapping the general range for magmatic or mantle $\delta^{34}S$ (0 ± 3%, Ohmoto, 1986; Seal, 2006). In addition, these values are markedly different from those of the fine-grained sedimentary pyrite in slate (+7.0 to +23.3‰) (Fig. 7a), suggesting the injection of magmatic sulfur. Similar conclusions have been presented to explain the formation of the Carlin-type gold deposits in Nevada, USA (Kesler et al., 2005; Barker et al., 2009). For example, Kesler et al. (2005) reported that the $\delta^{34}S$ values for pyrite in barren samples (−13 to +16‰) differ from those in mineralized samples (−1.0 to +3.0‰); the latter are interpreted as having a magmatic origin. The lack of a wide range of ^{34}S values in hydrothermal pyrite also suggests that contamination by sedimentary sulfur is not extensive. The injection of a magmatic component is also evidenced by the measured H and O isotopic signatures of the quartz in Stage 2 ($\delta^{18}O_{H2O}$ = 6.2 to 7.4‰, δD_{V-SMOW} = −72 to −52‰; Li et al., 2016) and Stage 3 ($\delta^{18}O_{H2O}$ = 6.9 to 8.1‰, δD_{V-SMOW} = −78 to −49‰; Li et al., 2016), as these values are restricted to the ranges of magmatic water.

(2) The accordance between the mineralization age and local tectono-magmatic setting supports a magmatic-hydrothermal origin. The $^{40}Ar/^{39}Ar$ age of muscovite (223.6 ± 5.3 Ma) is comparable to the zircon U–Pb ages for the granites in the XZMP (Fig. 1b, Table A1), suggesting synchronous magmatic and hydrothermal activity. For example, the Baimashan granite was mainly emplaced between ca. 223 and 204 Ma (Fig. 1b; Chen et al., 2007; Chu et al., 2012b; Fu et al., 2015).(see Table A2)

(3) Studies have shown that the surrounding sedimentary rocks (e.g., black shales) may represent a potential source of Au and S in some sediment-hosted orogenic gold deposits, given that sedimentary pyrite and organic matter (e.g., pyrobitumen) are reservoirs of Au (Chang et al., 2008; Large et al., 2007, 2011). In the Gutaishan deposit, the measured Au concentrations in sedimentary pyrite are mostly < 3.0 ppm (Fig. 7b), and no free gold is observed within sedimentary pyrite (Li et al., 2018; references therein). No organic matter (e.g., pyrobitumen) is found in the slate; thus, as Au may be transported in petroleum (Emsbo and Koenig, 2007; Large et al.,
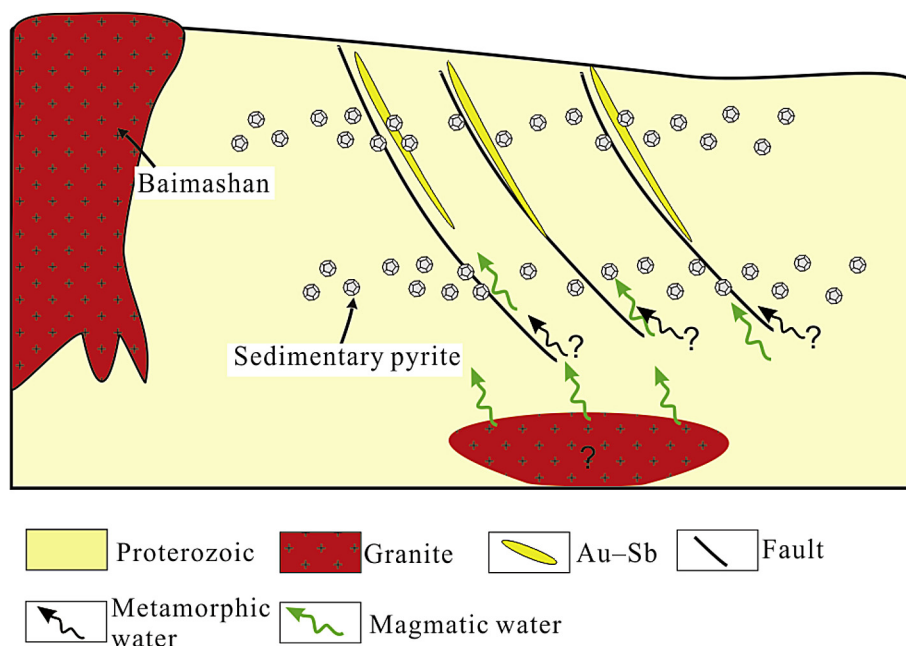
Fig. 8. Schematic diagram summarizing the proposed formation model for the Gutaishan deposit. See the text for an additional explanation.

2011), this precludes its possibility of hosting Au. The concentrations of Au in the Neoproterozoic strata are 3.6 ppb in the Lengjiaxi Group, 3.1 ppb in the Banxi Group, and 7.2 ppb in the Ediacaran (Ma et al., 2002); these values are only slightly higher than the concentrations of Au in the upper continental crust (1.5 ppb; Rudnick and Gao, 2003). Therefore, sulfide-bearing slate is unlikely to be the dominant source of Au. The occurrence of coarse-grained native gold and the higher concentrations of invisible gold in the pyrite and arsenopyrite in Stage 3 (Fig. 7b) suggest the late input of Au-rich fluid. (see Table A3)

Collectively, this evidence suggests that the wall-rock slate is unlikely to have been a major source of Au and S. Our schematic genetic model for the Gutaishan Au–Sb deposit (Fig. 8) highlights the potential role of magma emplacement. Geophysical evidence also supports the idea that a hidden intrusion may exist at depth around the Gutaishan deposit (Rao et al., 1993).

7.3. Implications for Late Triassic Au mineralization

In this study, we collected published data regarding the gold deposits surrounding the Baimashan batholith (Fig. 1b), namely, the Gutaishan deposit (223.6 ± 5.3 Ma, this study), the Xingfengshan deposit (hydrothermal titanite U–Pb: 206 ± 26 Ma), and the Chanziping and Daping Au deposits (fluid inclusion Rb–Sr isochron method: 205.6 ± 9.4 Ma and 204.8 ± 6.3 Ma, respectively; Li et al., 2008). All of these data are comparable and contemporaneous to the data on the published zircon U–Pb ages of the Baimashan granite (223 to 204 Ma; Fig. 1b, Table A1). The $\delta^{34}S$ values of sulfides from these deposits, namely, the Gutaishan deposit (−3.7 to +2.1‰ for the pyrite and arsenopyrite in Stage 3, this study) and the Chanziping Au deposit (−7.6 to +0.3‰ for pyrite and arsenopyrite; Luo et al., 1996), are mostly within the range of the values of magmatic sulfur. Moreover, the measured $\delta^{34}S$ values of sulfides from Au–Sb and Au deposits hosted in

slate, e.g., the sulfides from the Longshan Sb–Au deposit with values ranging from −2.1 to +4.6‰ (Luo, 1990), are broadly similar to those of magmatic sulfur, as reviewed in Hu et al. (2017b).

In addition to the close spatial and temporal relationships between the Baimashan granite and its surrounding deposits, a synthesis of published data suggests that other Late Triassic intrusions and their surrounding contemporary ore deposits have also been recognized in the XZMP (Fig. 1b). The mineralization age of the Fuzhuxi Au–Sb deposit is ∼209 Ma (Yao and Zhu, 1993), that of the Liaojiaping Au–Sb deposit is ∼200 Ma (Xiao et al., 1992) and that of the Zhazixi Sb–W deposit is ca. 227.3 ± 6.2 Ma (Wang et al., 2012). All of these data suggest that Triassic magmatism and Au–Sb ± W mineralization events occurred widely throughout the XZMP.

Xu et al. (2017) reviewed the gold mineralization events in the Jiangnan orogenic belt of South China (Fig. 1a), including the western and northwestern parts of the XZMP, and they proposed three gold mineralizing epochs: the Silurian-Devonian (423–397 Ma), the Jurassic (176–170 Ma) and the Early Cretaceous (144–130 Ma). Therefore, we highlight that Triassic gold mineralization constitutes another important gold mineralization epoch.

8. Conclusions

(1) The Gutaishan deposit formed ca. 223.6 ± 5.3 Ma, representing a case for an extensive Late Triassic Au mineralization event that occurred in the XZMP.

(2) The *in situ* sulfur isotope compositions of pyrite and arsenopyrite indicate a major contribution from magmatic sulfur. A magma-related genetic model may thus be suitable for the Gutaishan deposit.

Acknowledgements

Appendix

See Appendix Tables A1–A3.

Table A1
Summary of the ages of the Triassic granites in the Xiangzhong metallogenic province.

Name	Sample No.	Rock	Age (Ma)	Analytical method	Reference
Baimashan	BMS-01	Granite	214.3 ± 3.4	Zircon SIMS U–Pb	Fu et al., 2015
Baimashan	LFJ-01	Granite	209.3 ± 4.0	Zircon SIMS U–Pb	Fu et al., 2015
Baimashan	LZW-06	Granite	211.5 ± 4.2	Zircon SIMS U–Pb	Fu et al., 2015
Baimashan	SMP-01	Granite	215.3 ± 3.1	Zircon SIMS U–Pb	Fu et al., 2015
Baimashan	YBC-01	Granite	212.1 ± 3.3	Zircon SIMS U–Pb	Fu et al., 2015
Baimashan	D1060	Biotite granodiorite	224.1 ± 2.3	Zircon SHRIMP U–Pb	Li et al., 2014a
Baimashan	D1008	Biotite granodiorite	219.6 ± 2.6	Zircon SHRIMP U–Pb	Li et al., 2014a
Baimashan	D1025	Biotite monzogranite	213.8 ± 2.5	Zircon SHRIMP U–Pb	Li et al., 2014a
Baimashan	Ym132	Biotite monzogranite	215.9 ± 1.9	Zircon SHRIMP U–Pb	Li et al., 2014b
Baimashan	Ym134	Biotite monzogranite	212.2 ± 2.1	Zircon SHRIMP U–Pb	Li et al., 2014b
Baimashan	HH27-5	Granodiorite	217.0 ± 1.4	Zircon SIMS U–Pb	Qiu et al., 2014
Baimashan	HH29-5	Granite	217.8 ± 2.2	Zircon SIMS U–Pb	Qiu et al., 2014
Baimashan	HH31-8	Granodiorite	218.7 ± 1.5	Zircon SIMS U–Pb	Qiu et al., 2014
Baimashan	XF221	Hornblend granite	217 ± 2	Zircon SIMS U–Pb	Chu et al., 2012
Baimashan	06HG-69	Biotite monzogranite	223.3 ± 1.4	Zircon LA–ICPMS U–Pb	Luo et al., 2010
Baimashan	06HG-81	Biotite granodiorite	204.5 ± 2.2	Zircon LA–ICPMS U–Pb	Luo et al., 2010
Baimashan	HBMS-28	Biotite monzogranite	204.5 ± 2.8	Zircon LA–ICPMS U–Pb	Chen et al., 2007a,b
Baimashan	HBMS-20	Biotite granodiorite	209.2 ± 3.8	Zircon LA–ICPMS U–Pb	Chen et al., 2007a,b
Baimashan	HBMS-24	Two-mica monzogranite	204 ± 12	Zircon LA–ICPMS U–Pb	Chen et al., 2007a,b
Baimashan	02JSH03	Monzogranite	243 ± 3	Zircon SHRIMP U–Pb	Wang et al., 2005
Dashenshan	DSS12-8	Granodiorite	211 ± 3	Zircon SHRIMP U–Pb	Xu et al., 2014b
Dashenshan	DSS-8	Biotite monzogranite	224.3 ± 1.0	Zircon LA–ICPMS U–Pb	Zhang et al., 2012
Taojiang	04H-12–1	Granodiorites	218 ± 3	Zircon SHRIMP U–Pb	Xu et al., 2014a
Taojiang	XF17	Biotite granite	220 ± 2	Zircon SIMS U–Pb	Chu et al., 2012
Taojiang	09TJ-2e	Biotite granodiorite	216.2 ± 1.9	Zircon LA–ICPMS U–Pb	Wang et al., 2012
Taojiang	09TJ-2i	Biotite granodiorite	217.2 ± 1.3	Zircon LA–ICPMS U–Pb	Wang et al., 2012
Taojiang	10TJ-3	Biotite granodiorite	217.2 ± 1.3	Zircon LA–ICPMS U–Pb	Wang et al., 2012
Wawutang	12D01	Monzogranite	223.1 ± 2.1	Zircon LA–ICPMS U–Pb	Su et al., 2016
Wawutang	SH203-1	Biotite monzogranite	216.4 ± 2.4	Zircon SHRIMP U–Pb	Bai et al., 2016
Wawutang	SH209-1	Biotite granodiorite	215.3 ± 3.2	Zircon SHRIMP U–Pb	Bai et al., 2016
Wawutang	Ym135	Biotite monzogranite	217.7 ± 1.8	Zircon SHRIMP U–Pb	Li et al., 2014b
Wawutang	02DM05	Granite	235 ± 4	Zircon SHRIMP U–Pb	Wang et al., 2007
Wawutang	HWWT12-10	Granite	204 ± 3	Zircon LA–ICPMS U–Pb	Chen et al., 2007a,b
Weishan	QLS-01	Granite	213.9 ± 3.7	Zircon SIMS U–Pb	Fu et al., 2015
Weishan	XNF-01	Granite	217.9 ± 2.8	Zircon SIMS U–Pb	Fu et al., 2015
Weishan	XF205	Biotite monzogranite	222 ± 3	Zircon SIMS U–Pb	Chu et al., 2012
Weishan	HWS32b	Biotite monzogranite	227 ± 13	Biotite Rb-Sr	Ding et al., 2012
Weishan	W03	Biotite monzogranite	221.9 ± 5.8	Muscovite Rb-Sr	Ding et al., 2012
Weishan	HWS42	Biotite monzogranite	210.1 ± 3.3	Biotite Rb-Sr	Ding et al., 2012
Weishan	02LSH-05	Biotite monzonitic granite	210.6 ± 3.1	Zircon LA–ICPMS U–Pb	Peng et al., 2006
Weishan	HWS-36	Biotite monzogranite	211.0 ± 1.6	Zircon LA–ICPMS U–Pb	Ding et al., 2005
Weishan	HWS-40	Biotite monzogranite	215.7 ± 1.9	Zircon LA–ICPMS U–Pb	Ding et al., 2005
Weishan	02QSH06	Biotite monzogranite	244 ± 4	Zircon SHRIMP U–Pb	Wang et al., 2005
Xiema	09XM-3a	Biotite granodiorites	220.8 ± 3.8	Zircon LA–ICPMS U–Pb	Wang et al. 2015
Xiema	09XM-7a	Biotite granodiorites	216.2 ± 2.1	Zircon LA–ICPMS U–Pb	Wang et al., 2015
Xiema	01XM-01	Biotite monzonitic granite	217.8 ± 2.9	Zircon LA–ICPMS U–Pb	Peng et al., 2006
Ziyunshan	ZYS-5	Quartz monzonite	225.2 ± 1.7	Zircon SIMS U–Pb	Lu et al., 2017
Ziyunshan	ZYS-13	Two-mica granite	227.9 ± 2.2	Zircon SIMS U–Pb	Lu et al., 2017
Ziyunshan	ZYS-24	Quartz monzonite	225.6 ± 1.4	Zircon SIMS U–Pb	Lu et al., 2017
Ziyunshan	JZJ-02	Granite	223.2 ± 3.3	Zircon SIMS U–Pb	Fu et al., 2015
Ziyunshan	09XM-10	Biotite granodiorites	218.8 ± 2.1	Zircon LA–ICPMS U–Pb	Wang et al., 2015
Ziyunshan	09XM-11	Biotite granites	217.4 ± 3.1	Zircon LA–ICPMS U–Pb	Wang et al., 2015
Ziyunshan	10ZYS-05	Two-mica granites	219.9 ± 3.6	Zircon LA–ICPMS U–Pb	Wang et al., 2015
Ziyunshan	09ZYS-01	Granodiorite	222.5 ± 1.0	Zircon LA–ICPMS U–Pb	Liu et al., 2014
Ziyunshan	11ZYS-05	Biotite granite	222.3 ± 1.8	Zircon LA–ICPMS U–Pb	Liu et al., 2014
Ziyunshan	XF208	Biotite monzogranite	225 ± 2	Zircon SIMS U–Pb	Chu et al., 2012

Table A2
Characteristics of the analyzed samples from the Gutaishan deposit.

Sample No.	Stage	Description	Mine level	Sulfide(s)	Mineral characteristics
GTS-212	1	Thin sedimentary pyrite vein	520m	Py1a, Py1b	Py1a is generally small (< 3 μm), and form irregularly-shaped clusters of variable size ranging from tens to hundreds of μm. Py1bI overgrowths on Py1a, with the grain sizes mainly ranging from 50 to 150 μm
GTS-227	1	Thin sedimentary pyrite vein	280m	Py1a, Py1b	Fine-grained (10–20 μm) Py1a is enclosed by recrystallized subhedral pyrite assemblages (Py1bI). The grain sizes of Py1bI and Py1bII range from 50 to 100 μm. The anhedral Py1bII assemblages contain minor galena inclusions (few μm in size) and Py1bII varies from 500 to 1,000 μm in size
GTS-108	1	Thin sedimentary pyrite vein	280m	Py1a, Py1b, Apy1	Py1a is enclosed by recrystallized subhedral pyrite assemblages (Py1bI and Py1bII). Py1a is of 1 to 3 μm in size. The grain sizes of Py1bI and Py1bII are in the range of 20 to 50 μm and 100 to 1,000 μm respectively. The subhedral coarse-grained Apy1 grains are up to3,000 μm
GTS-114	2	Quartz -sulfide vein and adjacent sulfidation wallrock	430m	Py2a, Apy2	The porous euhedral Py2a grains range from 150 to 200 μm in size. The homogenous Apy2 within the quartz vein varies from 20 to 1,500 μm in size, and the porous Apy2 located in the adjacent wallrock ranges from 200 to 500 μm in size
GTS-123	2	Quartz -sulfide vein and adjacent sulfidation wallrock	360m	Py2a, Py2b, Py2c, Apy2	Pyrites are mainly located within the quartz vein and the Apy2 are within the wallrock. The porous euhedral Py2a is enclosed by Py2b, and late infilled by Py2c. Py2a within the quartz vein ranges from 50 to 100 μm in size. The subhedral Py2b ranges from 100 to 300 μm in size. The anhedral Py2c ranges from 20 to 100 μm in size. The Apy2 ranges from 50 to 400 μm in size
GTS-214	2	Quartz -sulfide vein and adjacent sulfidation wallrock	360m	Py2a, Py2b, Apy2	The porous anhedral Py2a is enclosed by Py4, and the latter coexists with Apy2. The Py2a ranges from 100 to 250 μm in size. The subhedral Py2b ranges from 50 to 1,500 μm in size. The homogeneous Apy2 ranges from 150 to 1,000 μm in size
GTS-107	3	Quartz -sulfide vein and adjacent sulfidation wallrock	280m	Py3a, Apy3a	The sericite-bearing Py3a coexists with homogeneous Apy3a. The Py3a grains have sizes ranging from 100 to 350 μm. The euhedral Apy3a ranges from 50 to 1,300 μm in size
GTS-208	3	Quartz -sulfide vein and adjacent sulfidation wallrock	520m	Py3a, Apy3a	The homogeneous Py3a coexists with homogeneous Apy3a. The subhedral Py3a ranges from 250 to 600 μm in size. The euhedral Apy3a ranges from 50 to 1,500 μm in size
GTS-201	3	Quartz -sulfide vein, contains native gold	410m	Py3a, Apy3a	The homogeneous euhedral Py3a coexists with subhedral Apy3a. The size of Py3a ranges is about 300 μm in size. The subhedral Apy3a ranges from 100 to 500 μm in size
GTS-225	3	Quartz -sulfide vein, contains native gold	430m	Py3b, Apy3b	The Py3b grains commonly sub- to anhedral, from 50 to 400 μm across, showing homogenous textures. Apy3b is subhedral to anhedral, from 50 to 500 μm across, and shows relatively uniform composition
GTS-154	3	Quartz -sulfide vein, contains native gold	520m	Py3c, Py3d	The Py3c is generally rounded, and shows characteristic oscillatory texture, with a porous core, 100 to 200 μm in size. The Py3d is anhedral, homogeneous, and generally 10–50 μm in size

Table A3

In situ sulfur isotope compositions of the pyrite and arsenopyrite in the Gutaishan deposit.

Sample No.	Stage	Textural sub-type	^{32}S (CPS)	Raw ^{34}S/^{32}S	± 2σ	δ^{34}S (‰, V-CDT)	± 2σ (internal)	± 2σ (external)	Au (ppm)			n
									Average	Min	Max	
GTS-212-2-2	1	Py1a	2.96E + 08	0.0442	5.13E − 06	11.3	0.12	0.36	1.8	0.8	4.6	15
GTS-212-7-1	1	Py1a	3.12E + 08	0.0441	4.39E − 06	8.5	0.10	0.36	1.8	0.8	4.6	15
GTS-212-7-3	1	Py1a	3.13E + 08	0.0441	5.47E − 06	9.0	0.12	0.36	1.8	0.8	4.6	15
GTS-227-2-1	1	Py1a	2.98E + 08	0.0441	3.57E − 06	9.1	0.08	0.35	1.8	0.8	4.6	15
GTS-227-2-2	1	Py1a	3.15E + 08	0.0443	5.24E − 06	14.1	0.12	0.36	1.8	0.8	4.6	15
GTS-108-1-5	1	Py1b	3.23E + 08	0.0443	4.04E − 06	14.0	0.09	0.57	2.6	1.2	3.8	5
GTS-108-1-6	1	Py1b	3.29E + 08	0.0447	8.07E − 06	23.3	0.18	0.59	2.6	1.2	3.8	5
GTS-212-2-3	1	Py1b	3.03E + 08	0.0440	5.84E − 06	7.0	0.13	0.37	0.3	0.0	0.9	15
GTS-212-2-4	1	Py1b	2.86E + 08	0.0440	6.29E − 06	7.3	0.14	0.37	0.3	0.0	0.9	15
GTS-227-2-3	1	Py1b	3.03E + 08	0.0445	5.71E − 06	18.3	0.13	0.37	0.2	0.0	0.5	12
GTS-227-2-6	1	Py1b	2.92E + 08	0.0441	5.49E − 06	8.1	0.12	0.36	0.4	0.2	0.8	6
GTS-214-9-1	2	Py2a	3.02E + 08	0.0436	5.74E − 06	− 3.2	0.13	0.37	1.6	0.4	4.0	7
GTS-214-9-2	2	Py2a	3.01E + 08	0.0436	5.41E − 06	− 2.7	0.12	0.36	1.6	0.4	4.0	7
GTS-214-3-1	2	Py2a	2.86E + 08	0.0436	4.58E − 06	− 2.5	0.10	0.36	1.6	0.4	4.0	7
GTS-214-3-2	2	Py2a	2.84E + 08	0.0436	4.34E − 06	− 1.4	0.10	0.36	1.6	0.4	4.0	7
GTS-123-12-1	2	Py2b	3.01E + 08	0.0440	6.21E − 06	5.7	0.14	0.58	1.6	0.9	5.6	9
GTS-123-12-2	2	Py2b	3.09E + 08	0.0437	7.02E − 06	1.0	0.16	0.59	1.6	0.9	5.6	9
GTS-123-12-3	2	Py2b	3.12E + 08	0.0437	4.79E − 06	0.0	0.11	0.58	1.6	0.9	5.6	9
GTS-123-12-4	2	Py2b	3.14E + 08	0.0438	5.49E − 06	1.4	0.12	0.58	1.6	0.9	5.6	9
GTS-123-12-5	2	Py2b	3.07E + 08	0.0438	4.73E − 06	1.5	0.11	0.58	1.6	0.9	5.6	9
GTS-214-9-3	2	Py2b	3.11E + 08	0.0436	5.87E − 06	− 2.6	0.13	0.37	0.5	0.0	1.8	10
GTS-214-9-4	2	Py2b	2.99E + 08	0.0437	6.63E − 06	0.1	0.15	0.37	0.5	0.0	1.8	10
GTS-214-9-5	2	Py2b	3.18E + 08	0.0436	4.69E − 06	− 2.1	0.11	0.36	0.5	0.0	1.8	10
GTS-214-9-6	2	Py2b	2.95E + 08	0.0436	5.41E − 06	− 2.4	0.12	0.36	0.5	0.0	1.8	10
GTS-123-9-1	2	Py2c	3.13E + 08	0.0438	4.62E − 06	1.8	0.10	0.58	3.9	0.6	15.9	11
GTS-123-9-2	2	Py2c	3.02E + 08	0.0439	5.33E − 06	3.8	0.12	0.58	3.9	0.6	15.9	11
GTS-123-9-3	2	Py2c	3.09E + 08	0.0438	3.65E − 06	1.2	0.08	0.57	3.9	0.6	15.9	11
GTS-123-9-4	2	Py2c	3.08E + 08	0.0438	6.32E − 06	2.3	0.14	0.58	3.9	0.6	15.9	11
GTS-123-9-5	2	Py2c	3.13E + 08	0.0437	4.99E − 06	− 0.3	0.11	0.58	3.9	0.6	15.9	11
GTS-107-2-4	3	Py3a	3.33E + 08	0.0437	6.44E − 06	− 0.1	0.15	0.58	3.1	0.2	17.4	11
GTS-107-2-5	3	Py3a	3.16E + 08	0.0437	4.52E − 06	− 0.2	0.10	0.57	3.1	0.2	17.4	11
GTS-201-1-7	3	Py3a	3.00E + 08	0.0437	5.06E − 06	− 1.1	0.11	0.36	3.0	0.6	6.9	12
GTS-201-1-8	3	Py3a	3.06E + 08	0.0436	4.29E − 06	− 2.2	0.10	0.36	3.0	0.6	6.9	12
GTS-208-5-1	3	Py3a	1.82E + 08	0.0435	8.41E − 06	− 1.7	0.19	0.64	4.0	0.6	14.2	11
GTS-208-5-2	3	Py3a	1.77E + 08	0.0435	1.07E − 05	− 2.0	0.24	0.65	4.0	0.6	14.2	11
GTS-225-4-6	3	Py3b	3.22E + 08	0.0437	3.93E − 06	− 0.8	0.09	0.35	12.3	2.0	27.3	13
GTS-225-4-7	3	Py3b	3.13E + 08	0.0436	4.70E − 06	− 1.6	0.11	0.36	12.3	2.0	27.3	13
GTS-225-4-8	3	Py3b	3.09E + 08	0.0436	4.03E − 06	− 1.9	0.09	0.35	12.3	2.0	27.3	13
GTS-225-4-9	3	Py3b	2.98E + 08	0.0437	5.34E − 06	− 0.3	0.12	0.36	12.3	2.0	27.3	13
GTS-154-1-1	3	Py3c	3.12E + 08	0.0437	4.99E − 06	0.1	0.11	0.36	14.6	2.1	51.0	11
GTS-154-1-3	3	Py3c	3.04E + 08	0.0437	5.19E − 06	− 1.0	0.12	0.36	14.6	2.1	51.0	11
GTS-154-1-4	3	Py3c	2.94E + 08	0.0437	6.54E − 06	− 1.2	0.15	0.37	14.6	2.1	51.0	11
GTS-154-1-5	3	Py3c	2.95E + 08	0.0437	6.41E − 06	− 1.0	0.15	0.37	14.6	2.1	51.0	11
GTS-154-5-1	3	Py3d	3.09E + 08	0.0438	4.06E − 06	2.1	0.09	0.35	1.4	0.2	6.1	8
GTS-154-5-2	3	Py3d	3.04E + 08	0.0437	5.13E − 06	0.5	0.12	0.36	1.4	0.2	6.1	8
GTS-154-5-3	3	Py3d	2.95E + 08	0.0437	4.89E − 06	0.6	0.11	0.36	1.4	0.2	6.1	8
GTS-154-5-4	3	Py3d	2.96E + 08	0.0437	6.61E − 06	0.9	0.15	0.37	1.4	0.2	6.1	8
GTS-154-5-5	3	Py3d	3.07E + 08	0.0437	5.91E − 06	0.9	0.13	0.37	1.4	0.2	6.1	8
GTS-114-1-1	2	Apy2	1.78E + 08	0.0434	9.57E − 06	− 2.8	0.22	0.75	13.0	0.7	30.2	7
GTS-114-1-2	2	Apy2	1.75E + 08	0.0434	1.05E − 05	− 3.3	0.24	0.75	13.0	0.7	30.2	7
GTS-214-9-7	2	Apy2	1.72E + 08	0.0434	1.00E − 05	− 5.9	0.23	0.65	13.1	0.2	85.9	14
GTS-214-8-1	2	Apy2	1.72E + 08	0.0434	9.92E − 06	− 5.9	0.22	0.65	13.1	0.2	85.9	14
GTS-214-8-2	2	Apy2	1.68E + 08	0.0434	7.08E − 06	− 5.5	0.16	0.63	13.1	0.2	85.9	14
GTS-107-2-1	3	Apy3a	1.92E + 08	0.0436	1.20E − 05	1.7	0.27	0.76	40.3	2.3	120.4	16
GTS-107-2-2	3	Apy3a	1.90E + 08	0.0435	8.53E − 06	0.5	0.19	0.74	40.3	2.3	120.4	16
GTS-107-2-3	3	Apy3a	1.85E + 08	0.0435	1.06E − 05	0.2	0.24	0.75	40.3	2.3	120.4	16
GTS-107-1-1	3	Apy3a	1.90E + 08	0.0436	1.04E − 05	1.1	0.24	0.75	40.3	2.3	120.4	16
GTS-208-5-3	3	Apy3a	3.05E + 08	0.0437	5.29E − 06	− 1.1	0.12	0.36	22.1	0.7	91.6	20
GTS-208-5-4	3	Apy3a	2.96E + 08	0.0437	5.07E − 06	− 1.0	0.11	0.36	22.1	0.7	91.6	20
GTS-201-1-1	3	Apy3a	1.74E + 08	0.0436	8.93E − 06	− 1.3	0.20	0.64	88.7	2.7	203.4	16
GTS-201-1-2	3	Apy3a	1.71E + 08	0.0435	1.21E − 05	− 2.2	0.27	0.67	88.7	2.7	203.4	16
GTS-201-1-3	3	Apy3a	1.76E + 08	0.0435	1.12E − 05	− 3.7	0.25	0.66	88.7	2.7	203.4	16
GTS-201-1-4	3	Apy3a	1.76E + 08	0.0435	9.64E − 06	− 3.1	0.22	0.65	88.7	2.7	203.4	16
GTS-225-4-1	3	Apy3b	1.77E + 08	0.0436	8.66E − 06	− 1.3	0.20	0.64	102.3	2.9	367.0	15
GTS-225-4-2	3	Apy3b	1.78E + 08	0.0435	7.15E − 06	− 1.7	0.16	0.63	102.3	2.9	367.0	15
GTS-225-4-3	3	Apy3b	1.78E + 08	0.0436	8.61E − 06	− 1.5	0.20	0.64	102.3	2.9	367.0	15
GTS-225-4-4	3	Apy3b	1.77E + 08	0.0435	8.63E − 06	− 2.2	0.20	0.64	102.3	2.9	367.0	15

Note: The 'n' represents the number of spots measured by LA–ICP–MS by Li et al. (2018).

References

Bai, D., Wu, N.J., Zhong, X., Jia, P.Y., Xiong, X., Huang, W.Y., 2016. Geochronology, petrogenesis and tectonic setting of Indosinian Wawutang granites, southwestern Hunan province. Geotect. Metall. 40, 1075–1091 (in Chinese with English abstract).

Baker, 2002. Emplacement depth and carbon dioxide-rich fluid inclusions in intrusion-related gold deposits. Econ. Geol. 97, 1111–1117.

Barker, S.L.L., Hickey, K.A., Cline, J.S., Dipple, G.M., Kilburn, M.R., Vaughan, J.R., Longo, A.A., 2009. Uncloaking invisible gold: use of nanoSIMS to evaluate gold, trace elements, and sulfur isotopes in pyrite from Carlin-type gold deposits. Econ. Geol. 104, 897–904.

Battaglia, F., 1999. Applying X-ray geothermometer diffraction to a chlorite. Clays Clary Mineral. 47, 54–63.

Chang, Z.S., Large, R.R., Maslennikov, V., 2008. Sulfur isotopes in sediment-hosted orogenic gold deposits: Evidence for an early timing and a seawater sulfur source. Geology 36, 971–974.

Chen, W.F., Chen, P.R., Huang, H.Y., Ding, X., Sun, T., 2007. Geochronological and geochemical study of Baimashan granite and its xenoliths. Sci. China Ser. D 37, 873–893 (in Chinese).

Chen, W.F., Chen, P.R., Huang, H.Y., Ding, X., Sun, T., 2007a. Chronological and geochemical studies of granite and enclave in Baimashan pluton, Hunan, south china. Sci. China 50, 1606–1627.

Chen, W.F., Chen, P.R., Zhou, X.M., Huang, H.Y., Ding, X., Sun, T., 2007b. Single zircon LA–ICP–MS U-Pb dating of the Guandimiao and Wawutang granitic plutons in Hunan, south China and its petrogenetic significance. Acta Geol. Sin. 81, 81–89.

Chen, L., Li, X.H., Li, J.W., Hofstra, A.H., Liu, Y., Koenig, A.E., 2015. Extreme variation of sulfur isotopic compositions in pyrite from the Qiuling sediment-hosted gold deposit, West Qinling orogen, central China: an *in-situ* SIMS study with implications for the source of sulfur. Miner. Deposita 50, 643–656.

Chu, Y., Faure, M., Lin, W., Wang, Q., Ji, W.B., 2012a. Tectonics of the Middle Triassic intracontinental Xuefengshan belt, south china: new insights from structural and chronological constraints on the basal décollement zone. Int. J. Earth Sci. 101, 2125–2150.

Chu, Y., Lin, W., Faure, M., Wang, Q., Ji, W., 2012b. Phanerozoic tectonothermal events of the Xuefengshan Belt, central South China: implications from U-Pb age and Lu–Hf determinations of granites. Lithos 150, 243–255.

Chu, Y., Lin, W., Faure, M., Wang, Q.C., Ji, W.B., 2012. Phanerozoic tectonothermal events of the Xuefengshan belt, central south China: implications from U-Pb age and Lu–Hf determinations of granites. Lithos 150, 243–255.

Cook, N.J., Chryssoulis, S.L., 1990. Concentrations of "invisible gold" in the common sulfides. Can. Mineral. 28, 1–16.

Crowe, D.E., Vaughan, R.G., 1996. Characterization and use of isotopically homogeneous standards for in situ laser microprobe analysis of $^{34}S/^{32}S$ ratios. Am. Mineral. 81, 187–193.

Ding, X., Chen, P.R., Chen, W.F., Huang, H.Y., Zhou, X.M., 2005. A-ICPMS zircon U–Pb dating for the Weishan pluton in Hunan province and implications on petrogenesis. Sci. China Ser. D Earth Sci. 35, 606–616 (in Chinese).

Ding, X., Sun, W.D., Wang, F.Y., Chen, L.L., Li, Q.L., Chen, F.K., 2012. Single-grain mica Rb–Sr isochron ages and mineral chemistry for the Weishan pluton in Hunan province and implications on petrogenesis and mineralization of Mesozoic composite granite in south china. Acta Petrol. Sin. 28, 3823–3840 (in Chinese with English abstract).

Emsbo, P., Koenig, A.E., 2007. Transport of Au in petroleum: Evidence from the northern Carlin Trend, Nevada: Digging Deeper, Biennial SGA Meeting, 9th, Dublin, Society for Geology Applied to Mineral Deposits. Proceedings, 695 − 698.

Faure, M., Shu, L.S., Wang, B., Charvet, J., Choulet, F., Monié, P., 2009. Intracontinental subduction: a possible mechanism for the Early Paleozoic Orogen of SE China. Terra Nova 21, 360–368.

Fu, S.L., Hu, R.Z., Bi, X.W., Chen, Y.W., Yang, J.H., Huang, Y., 2015. Origin of Triassic granites in central Hunan province, South China: constraints for zircon U-Pb ages and Hf–O isotopes. Int. Geol. Rev. 57, 97–111.

Fu, S.L., Hu, R.Z., Bi, X.W., Chen, Y.W., Yang, J.H., Huang, Y., 2015. Origin of Triassic granites in central Hunan province, South China: Constraints for zircon U-Pb ages and Hf–O isotopes. Int. Geol. Rev. 57, 97–111.

Gao, P., Zheng, Y.F., Zhao, Z.F., 2017. Triassic granites in South China: A geochemical perspective on their characteristics, petrogenesis, and tectonic significance. Earth Sci. Rev. 173, 266–294.

Geological map of Hunan province, the People's Republic of China 1: 500000., 2010. Geological Publishing House, Beijing (in Chinese).

Goldfarb, R.J., Miller, M.L., Ebert, S.W., Marsh, E.E., Petsel, S.A., Miller, L.D., Bradley, D., Johnson, C., Mcclelland, W., 2004. The late cretaceous Donlin Creek gold deposit, southwestern Alaska: controls on epizonal ore formation. Econ. Geol. 99, 643–671.

Goldfarb, R.J., Baker, T., Dubé, B., Groves, D.I., Hart, C.J.R., Gosselin, P., 2005. Distribution, character, and genesis of gold deposits in metamorphic terranes. Econ. Geol. 100th Anniv. 407–450.

Groves, D.I., Goldfarb, R.J., Gebre-Mariam, M., Hagemann, S.G., Robert, F., 1998. Orogenic gold deposits—a proposed classification in the context of their crustal distribution and relationship to other gold deposit types. Ore Geol. Rev. 13, 7–27.

Groves, D.I., Goldfarb, R.J., Robert, F., Hart, C.J.R., 2003. Gold deposits in metamorphic belts: overview of current understanding, outstanding problems, future research, and exploration significance. Econ. Geol. 98, 1–29.

Hu, R.Z., Fu, S.L., Xiao, J.F., 2016. Major scientific problems on low-temperature metallogenesis in South China. Acta Petrol. Sin. 32, 3239–3251 (in Chinese with English abstract).

Hu, R.Z., Chen, W.T., Xu, D.R., Zhou, M.F., 2017a. Reviews and new metallogenic models of mineral deposits in South China: An introduction. J. Asian Earth Sci. 137, 1–8.

Hu, R.Z., Fu, S.L., Huang, Y., Zhou, M.F., Fu, S.H., Zhao, C.H., Wang, Y.J., Bi, X.W., Xiao, J.F., 2017b. The giant South China Mesozoic low-temperature metallogenic domain: reviews and a new geodynamic model. J. Asian Earth Sci. 137, 9–34.

Hu, R.Z., Zhou, M.F., 2012. Multiple Mesozoic mineralization events in South China–an introduction to the thematic issue. Miner. Deposita 47, 579–588.

Ireland, T.R., Schram, N., Holden, P., Lanc, P., Ávila, J., Armstrong, R., Amelin, Y., Latimore, A., Corrigan, D., Clement, S., Foster, J.J., Compston, W., 2014. Charge-mode electrometer measurements of S-isotopic compositions on Shrimp-SI. Int. J. Mass Spectrom. 359, 26–37.

Kerrich, R., Cassidy, K.F., 1994. Temporal relationships of lode gold mineralization to accretion, magmatism, metamorphism and deformation–Archean to present: a review. Ore Geol. Rev. 9, 263–310.

Kesler, S.E., Riciputi, L.C., Ye, Z., 2005. Evidence for a magmatic origin for Carlin-type gold deposits: isotopic composition of sulfur in the Betze-post-screamer deposit, Nevada, USA. Mineral Deposit. 40, 127–136.

Kuiper, Y.D., 2002. The interpretation of inverse isochron diagrams in 40Ar/39Ar geochronology. Earth Planet. Sci. Lett. 203, 499–506.

Lang, J., Baker, T., 2001. Intrusion-related gold systems: the present level of understanding. Miner. Deposita 36, 477–489.

Large, R.R., Maslennikov, V.V., Robert, F., Danyushevsky, L.V., Chang, Z.S., 2007. Multistage sedimentary and metamorphic origin of pyrite and gold in the giant Sukhoi Log deposit, Lena gold province, Russia. Econ. Geol. 102, 1233–1267.

Large, R.R., Bull, S.W., Maslennikov, V.V., 2011. A carbonaceous sedimentary source-rock model for Carlin-type and orogenic gold deposits. Econ. Geol. 106, 331–358.

Lee, J.Y., Marti, K., Severinghaus, J.P., Kawamura, K., Yoo, H.S., Lee, J.B., Kim, J.S., 2006. A redetermination of the isotopic abundances of atmospheric Ar. Geochim. Cosmochim. Acta 70, 4507–4512.

Li, H.Q., Wang, D.H., Chen, F.W., Mei, Y.P., Cai, H., 2008. Study on chronology of the Chanziping and Daping gold deposit in Xuefeng Mountains, Hunan province. Acta Geol. Sin. 82, 900–905.

Li, W., Xie, G.Q., Zhang, Z.Y., Zhang, X.K., 2016. Constraint on the genesis of Gutaishan gold deposit: evidence from fluid inclusion and C-H–O isotopes. Acta Petrol. Sin. 32, 3489–3506 (in Chinese with English abstract).

Li, W., Cook, N.J., Xie, G.Q., Mao, J.W., Ciobanu, C.L., Li, J.W., Zhang, Z.Y., 2018. Textures and trace element signatures of pyrite and arsenopyrite from the Gutaishan Au–Sb deposit, South China. Miner Deposita. https://doi.org/10.1007/s00126-018-0826-0.

Li, G.L., Wang, X.H., Yang, J., Liu, T.Y., 2014a. SHRIMP ages for the Baimashan batholith, Hunan province, and its geological significance. Land Resour. Herald 5, 62–65 (in Chinese).

Li, J.H., Zhang, Y.Q., Xu, X.B., Li, H.L., Dong, S.W., Li, T.D., 2014b. SHRIMP U-Pb dating of zircons from the Baimashan Longtan super-unit ad Wawutang granites in Hunan province and its geological implication. J. Jilin Univ. Earth Sci. Ed. 44, 158–175 (in Chinese with English abstract).

Liu, K., Mao, J.R., Zhao, X.L., Ye, H.M., Hu, Q., 2014. Geological and Geochemical characteristics and genetic significance of the Ziyunshan pluton in Hunan province. Acta Geol. Sin. 88, 208–227 (in Chinese with English abstract).

Liu, P.C., Tang, Q.C., Li, H.C., 2008. Geological characteristics, enrichment laws and prospecting direction of gold-antimony deposit in Longshan deposits of Hunan. Geol. Prospect. 44, 31–38 (in Chinese with English abstract).

Lu, Y.L., Peng, J.T., Yang, J.H., Hu, A.X., Li, Y.K., Tan, H.Y., Xiao, Q.Y., 2017. Petrogenesis of the Ziyunshan pluton in central Hunan, south China: Constraints from zircon U-Pb dating, element geochemistry and Hf–O isotopes. Acta Petrol. Sin. 33, 1705–1728 (in Chinese with English abstract).

Ludwig, K.R., 2003. User's manual for Isoplot 3.00: a geochronological toolkit for Microsoft Excel, Kenneth R. Ludwig, v. 4.

Luo, X.L., 1990. On the source of ore-forming substances of Precambrian gold deposits in Hunan province. J. Gulin College Geol. 10, 13–26 (in Chinese with English abstract).

Luo, X.Q., 1996. Mineralization and prospecting guide of Chanziping gold deposit in Hunan. Hunan Geol. 15, 33–38.

Luo, Z.G., Wang, Y.J., Zhang, F.F., Zhang, A.H., Zhang, Y.Z., 2010. LA–ICPMS zircon ages for the Indosinian Jintan and Baimashan granites and their geological implication. Geotecton. Metall. 34, 282–290 (in Chinese).

Ma, D.S., Pan, J.Y., Xie, Q.L., He, J., 2002. Ore source of Sb (Au) deposits in center Hunan: I. evidences of trace elements and experimental geochemistry. Mineral Deposits. 3, 366–376 (in Chinese with English abstract).

Mao, J.W., Cheng, Y.B., Chen, M.H., Pirajno, F., 2013. Major types and time–space distribution of Mesozoic ore deposits in South China and their geodynamic settings. Mineral Deposita. 48, 267–294.

Mark, D.F., de Stuart, F.M., Podesta, M., 2011. New high-precision measurements of the isotopic composition of atmospheric argon. Geochim. Cosmochim. Acta 75, 7494–7501.

Marsh, E.E., Goldfarb, R.J., Hart, C.J.R., Johnson, C.A., 2003. Geology and geochemistry of the Clear Creek intrusion-related gold occurrences, Tintina gold province, Yukon, Canada. Can. J. Earth Sci. 40, 681–699.

McDougall, I., Harrison, T.M., 1999. Geochronology and Thermochronology by the $^{40}Ar/^{39}Ar$ Method. Oxford University Press, Oxford.

Morelli, R., Creaser, R.A., Seltmann, R., Stuart, F.M., Selby, D., Graupner, T., 2007. Age and source constraints for the giant Muruntau gold deposit, Uzbekistan, from coupled Re-Os-He isotopes in arsenopyrite. Geology 35, 795–798.

Ohmoto, H., 1986. Stable isotope geochemistry of ore deposits. Rev. Mineral. 16, 491–559.

Peng, J.T., Hu, R.Z., Burnard, P.G., 2003. Samarium–neodymium isotope systematics of hydrothermal calcite from the Xikuangshan antimony deposit (Hunan, China): the potential of calcite as a geochronometer. Chem. Geol. 200, 129–136.

Peng, B.X., Wang, Y.J., Fan, W.M., Peng, T.P., Liang, X.Q., 2006. LA–ICPMS zircon U-Pb

dating for three Indosinian granitic plutons from central Hunan and western Guangdong provinces and its petrogenetic implications. Acta Geol. Sin. 80, 660–669.

Peterson, E.C., Mavrogenes, J.A., 2014. Linking high-grade gold mineralization to earthquake-induced fault valve processes in the Porgera gold deposit, Papua New Guinea. Geology 42, 383–386.

Phillips, D., Matchan, E.L., 2013. Ultra-high precision ^{40}Ar/^{39}Ar ages for Fish Canyon Tuff and Alder Creek Rhyolite sanidine: New dating standards required? Geochim. Cosmochim. Acta 121, 229–239.

Phillips, D., Matchan, E.L., Honda, M., Kuiper, K.F., 2017. Astronomical calibration of ^{40}Ar/^{39}Ar reference minerals using high-precision, multi-collector (ARGUSVI) mass spectrometry. Geochim. Cosmochim. Acta 196, 351–369.

Phillips, G.N., Powell, R., 2010. Formation of gold deposits-a metamorphic devolatilization model. J. Metamorph. Geol. 28, 689–718.

Qiu, L., Yan, D.P., Zhou, M.F., Arndt, N.T., Tang, S.L., Qi, L., 2014. Geochronology and geochemistry of the late Triassic Longtan pluton in south china: termination of the crustal melting and Indosinian orogenesis. Int. J. Earth Sci. 103, 649–666.

Rao, J.R., Wang, J.H., Cao, Y.Z., 1993. Deep structure in Hunan. Hunan Geol. 12 (S1), 1–101 (in Chinese with English abstract).

Rice, C.M., Mark, D.F., Selby, D., Neilson, J.E., Davidheiser-Kroll, B., 2016. The age and geological setting of quartz vein-hosted gold mineralization at Curraghinalt, norther Ireland: implications for genesis and classification. Econ. Geol. 111, 127–150.

Ridley, J.R., Diamond, L.W., 2000. Fluid chemistry of orogenic lode gold deposits and implications for genetic models. Rev. Econ. Geol. 13, 141–162.

Robert, F., Brommecker, R., Bourne, B.T., Dobak, P.J., McEwan, C.J., Rowe, R.R., Zhou, X., 2007. Models and exploration methods for major gold deposit types. Ore Deposits Explor. Technol. 7, 691–711.

Rudnick, R.L., Gao, S., 2003. Composition of the continental crust. Treat. Geochem. 3, 1–64.

Seal, R.R.I., 2006. Sulfur isotope geochemistry of sulfide minerals. Rev. Mineral. Geochem. 61, 633–677.

Selby, D., Creaser, R.A., Heaman, L.M., Hart, C.J., 2003. Re-Os and U-Pb geochronology of the Clear Creek, Dublin Gulch, and Mactung deposits, Tombstone gold belt, Yukon, Canada: Absolute timing relationships between plutonism and mineralization. Can. J. Earth Sci. 40, 1839–1852.

Sillitoe, R.H., Thompson, J., 1998. Intrusion-related vein gold deposits: Types, tectono-magmatic settings and difficulties of distinction from orogenic gold deposits. Resour. Geol. 48, 237–250.

Steiger, R.H., Jager, E., 1977. Subcommission on geochronology — convention on use of decay constants in geochronology and cosmochronology. Earth Planet. Sci. Lett. 36, 359–362.

Su, K.M., Lv, S.J., Kong, L.B., Yang, F.Q., Xiang, J.F., 2016. Geological characteristics, metallogentic regularity and model of quartz vein type tungsten deposits in Chongyangping, Hunan province. Mineral Deposits 35, 902–912 (in Chinese with English abstract).

Tanner, D., Henley, R.W., Mavrogenes, J.A., Holden, P., 2016. Sulfur isotope and trace element systematics of zoned pyrite crystals from the El Indio Au–Cu–Ag deposit, Chile. Contrib. Mineral. Petrol. 171, 33.

Thompson, J., Newberry, R.J., 2000. Gold deposits related to reduced granitic intrusions. Rev. Econ. Geol. 13, 377–400.

Wang, Y.L., Chen, Y.C., Wang, D.H., Xu, Y., Chen, Z.H., 2012. Scheelite Sm-Nd dating of the Zhazixi W-Sb deposit in Hunan and its geological significance. Geol. China 39, 1339–1344 (in Chinese with English abstract).

Wang, K.X., Chen, P.R., Ling, H.F., Zhao, K.D., Yu, Z.Q., 2012. Magma mingling and

chemical diffusion in the Taojiang granitoids in the Hunan province, China: Evidences from petrography, geochronology and geochemistry. Mineral. Petrol. 106, 243–264.

Wang, K.X., Chen, W.F., Chen, P.R., Ling, H.F., Huang, H., 2015. Petrogenesis and geo-dynamic implications of the Xiema and Ziyunshan plutons in Hunan province, south China. J. Asian Earth Sci. 111, 919–935.

Wang, Y.J., Zhang, Y.H., Fan, W.M., Peng, T.P., 2005. Structural signatures and 40Ar/39Ar geochronology of the Indosinian Xuefengshan transpressive belt, South China Interior. J. Struct. Geol. 27, 985–998.

Wang, Y.J., Fan, W.M., Liang, X.Q., Peng, T.P., Shi, Y.R., 2005. SHRIMP zircon U-Pb geochronology of Indosinian granites in Hunan province and its petrogenetic implications. Chin. Sci. Bull. 50, 1395–1403.

Wang, Y.J., Fan, W.M., Sun, M., Liang, X.Q., Zhang, Y.H., Peng, T.P., 2007. Geochronlogical, geochemical and geothermal constraints on petrogenesis of the Indosinian peraluminous granites in the South China Block: a case study in Hunan province. Lithos 96, 475–502.

Wang, Y.J., Fan, W.M., Sun, M., Liang, X.Q., Zhang, Y.H., Peng, T.P., 2007. Geochronological, geochemical and geothermal constraints on petrogenesis of the Indosinian peraluminous granites in the south china block: A case study in the Hunan province. Lithos 96, 475–502.

Wang, X.L., Zhou, J.C., Griffin, W.L., Zhao, G.C., Yu, J.H., Qiu, J.S., Zhang, Y.J., Xing, G.F., 2014. Geochemical zonation across a Neoproterozoic orogenic belt: isotopic evidence from granitoids and metasedimentary rocks of the Jiangnan orogen, China. Precambr. Res. 242, 154–171.

Xiao, Q.M., Zeng, D.R., Jin, F.Q., Yang, M.Y., Yang, Z.F., 1992. Time-space distribution feature and exploration guide of China's Sb deposits. Geol. Prospect. 12, 9–14 (in Chinese with English abstract).

Xie, G.Q., Mao, J.W., Bagas, L., Fu, B., Zhang, Z.Y., 2018b. Mineralogy and titanite geochronology of the Caojiaba W deposit, Xiangzhong metallogenic province, southern China: implications for a distal reduced skarn W formation. Miner. Deposita. https://doi.org/10.1007/s00126-018-0816-2.

Xie, G.Q., Mao, J.W., Li, W., Fu, B., Zhang, Z.Y., 2018a. Granite-related Yangjiashan tungsten deposit, southern China. Miner. Deposita. https://doi.org/10.1007/s00126-018-0805-5.

Xu, D.R., Deng, T., Chi, G.X., Wang, Z.L., Zou, F.H., Zhang, J.L., Zou, S.H., 2017. Gold mineralization in the Jiangnan orogenic belt of south china: geological, geochemical and geochronological characteristics, ore deposit-type and geodynamic setting. Ore Geol. Rev. 88, 565–618.

Xu, H., Ma, C., Zhao, J., Zhang, J., 2014a. Magma mixing generated Triassic I-type granites in south china. J. Geol. 122, 329–351.

Xu, H., Ma, C., Zhao, J., Zhang, J., 2014b. Petrogenesis of Dashenshan I-type granodiorite: implications for Triassic crustal-mantle interaction, south China. Int. Geol. Rev. 56, 332–350.

Xue, Y.M., Campbell, I., Ireland, T.R., Holden, P., Armstrong, R., 2013. No mass-in-dependent sulfur isotope fractionation in auriferous fluids supports a magmatic origin for Archean gold deposits. Geology 41, 791–794.

Yao, Z.K., Zhu, R.B., 1993. Polygenetic compound model for the Fuzhuxi gold deposit of Hunan Province and its prospecting. Geotect. Metall. 17, 199–209 (in Chinese with English abstract).

Zhang, L., Peng, J., Zhang, D., Hu, A.X., Yang, J.H., 2012. Geochemistry and petrogenesis of the Indosinian Dashenshan granite, western Hunan, south china. Geotecton. Metall. 36, 137–148 (in Chinese with English abstract).